

c0014 Dynamic Vascular Optical Tomographic Imaging for Peripheral Artery Disease and Breast Cancer

Andreas H. Hielscher^{1,2,3}, Alessandro Marone¹, Mirella L. Altoé¹,
Danielle R. Bajakian⁴, Dawn L. Hershman⁵, Hyun K. Kim³

¹DEPARTMENT OF BIOMEDICAL ENGINEERING, COLUMBIA UNIVERSITY, 1210 AMSTERDAM AVE., MC8904, NEW YORK, NY 10027, UNITED STATES; ²DEPARTMENT OF ELECTRICAL ENGINEERING, COLUMBIA UNIVERSITY, 500 WEST 120TH STREET, MUDD 1310, NEW YORK, NY 10027, UNITED STATES; ³DEPARTMENT OF RADIOLOGY, COLUMBIA UNIVERSITY MEDICAL CENTER, NEW YORK, NY 10032, UNITED STATES; ⁴DEPARTMENT OF SURGERY - DIVISION OF VASCULAR SURGERY AND ENDOVASCULAR INTERVENTIONS, COLUMBIA UNIVERSITY MEDICAL CENTER, HERBERT IRVING PAVILION, 161 FORT WASHINGTON AVENUE, NEW YORK, NY 10032, UNITED STATES; ⁵DEPARTMENTS OF MEDICINE AND EPIDEMIOLOGY, HERBERT IRVING COMPREHENSIVE CANCER CENTER, COLUMBIA UNIVERSITY MEDICAL CENTER, 161 FORT WASHINGTON, NEW YORK, NY 10032, UNITED STATES

s0010 1. Introduction

p0015 Similar to magnetic resonance imaging (MRI), where particular settings of radiofrequency pulses and gradients result in a particular image appearance, optical tomographic imaging can be performed in various different modes. For example, optical imaging systems can be divided into three different categories, time-domain (TD) systems, frequency-domain (FD) devices, and steady-state-domain (SSD) instrumentation [1,2]. Time-resolved systems inject very short light pulses into the tissue. Traveling through the tissue, the light pulses are attenuated and broadened in time, which can be measured with the appropriate detectors. In FD systems, the source strength is sinusoidally modulated, typically between 100 and 1000 MHz, which results in the propagation of so-called photon-density waves inside the tissue. The data acquisition consists of measuring amplitude differences and phase shifts between the incident wave and the detected wave. SSD systems employ light sources that are constantly delivering the same amount of energy to the tissue and the time-independent intensities are measured at the detectors.

p0020 Each of these modalities requires a different hardware and poses different challenges to the image reconstruction process. The information content as well as complexity of hardware and imaging software increases from SSD to FD and TD systems. The obtainable

354 NEUROPHOTONICS AND BIOMEDICAL SPECTROSCOPY

spatial resolution, given the same number of sources and detectors, ~~is thought to~~ increase from SSD to FD to TD systems. On the other hand, SSD systems allow for much faster data acquisition than TD systems. While SSD systems allow for data acquisition rates for one source and one detector of up to 8 kHz, FD systems are currently limited to $\sim 10\text{--}400$ Hz, and TD systems typically less than 1 Hz [3]. This makes SSD systems the ideal systems to look at fast physiological changes, such as hemodynamic changes in the brain or limbs. Time-resolved systems take typically more than 1 min, and rapid changes such as hemodynamic responses to stimuli cannot be imaged.

p0025 An issue that affects all three optical imaging modalities is the problem of obtaining absolute optical properties rather than changes in optical properties only. Typically, absolute values are harder to obtain than relative changes, since absolute attenuation needs to be measured. In practice this has proven to be difficult, even though some groups have developed careful calibration schemes and numerical methods and have performed first quantitative hemoglobin tomography studies [4–6]. These studies, however, have been limited to numerical problems and optical tomographic breast imaging. Most of currently available optical devices employed for brain imaging only provide measures of changes or differences with respect to a reference material or reference physiological state (rest vs. activity). An example is a measurement of optical properties during a breath-hold experiment. The patient is monitored before the breath hold. With the start of the breath hold the measured optical signals will change, and these changes can then be used to determine changes in oxyhemoglobin (HbO_2) and deoxyhemoglobin (Hb). However, since the absolute HbO_2 and Hb concentration were not known at the start of the experiments, the absolute concentrations are also not known afterward. Absolute measurements are difficult to obtain because the coupling coefficient between tissue and fibers, and also losses in optical fibers due to different bending and coupling into the detectors are difficult to determine. Therefore the error in absolute measurements ($\sim 1\%$, see e.g., Ref. [7]), even when carefully calibrated, is typically larger than the error in relative measurement schemes, where one can determine changes in transmitted light intensities with an accuracy of approximately $\sim 0.01\%$ [3].

p0030 In this chapter, we report on some recent clinical advances employing relative measurement schemes. In particular, we explore the performance of systems that gather optical tomographic imaging data on a subsecond scale over several minutes. Because of the fast data acquisition, all currently existing systems operate in the SSD. These so-called dynamic optical tomographic imaging systems are ideally suited to explore vascular reactivity and have increasingly been used in imaging of the brain [8], breast [9–13], joints [14,15], and peripheral arteries [16–19]. While other chapters have focused on advances in brain imaging, we show the potential of dynamic vascular optical tomographic imaging (VOTI) in the fields of peripheral artery disease (PAD) and breast cancer. In particular, analyzing results from two clinical studies, we determined that VOTI can diagnose PAD with high sensitivity and specificity. This holds true even for diabetic patients, for whom current diagnostic methods struggle to correctly assess the disease. Furthermore, we found that dynamic VOTI can potentially be used to

distinguish responders from non-responders to months of neoadjuvant chemotherapy as early as 2 weeks after treatment initiation. If confirmed in a larger prospective clinical trial, patients could be spared harmful side effects from an inefficient therapy, and alternative treatment approaches could be implemented.

s0015 2. Peripheral Artery Disease

s0020 2.1 Introduction

p0035 Peripheral artery disease (PAD), also called peripheral vascular disease (PVD), is a circulatory condition in which narrowed blood vessels reduce blood flow to the limbs. The narrowing of arteries is caused by plaque accumulation (fatty deposits and calcium) in the vascular walls. Often the first symptom of PAD is pain in the leg, particularly when walking. This so-called claudication becomes worse as the disease progresses, and the distance that a patient can walk without pain becomes shorter and shorter. In later stages, the pain becomes severe and present even at rest. Untreated, the disease eventually leads to formation of foot wounds or ulcerations, which can subsequently lead to infection of the wound and tissue loss (gangrene), and amputation.

p0040 PAD affects approximately 12 million individuals in the United States and is associated with significant morbidity and mortality [20]. Every year, PAD is responsible for over 2,750,000 office visits, 10% of which result in hospital admissions. Approximately 45,000 PAD patients die from this disease annually [21]. Furthermore, patients with PAD have an increased risk of stroke and myocardial infarction and show a twofold increase in the risk of death from cardiovascular disease [22]. Lower extremity percutaneous transluminal angioplasty or bypass surgery is performed when advanced stages are reached and limb-threatening ischemia occurs. Once gangrene develops, amputation is necessary to prevent infected and dying tissues from causing septicemia. Therefore, accurate and timely diagnosis of PAD is crucial in the prevention of further health consequences.

p0045 The first-line diagnostic test for determination of PAD is the ankle brachial index (ABI) [22]. The ABI is calculated by measuring the maximum systolic blood pressure at the ankle and dividing it by the systolic blood pressure in the brachial artery in the upper arm. In healthy individuals ABI values range between 0.9 and 1. Values less than 0.9 identify patients with some form of vascular occlusions or stenoses in a major leg artery. Most patients with symptoms of claudication will have an ABI between 0.5 and 0.8, and those with more severe symptoms such as rest pain will generally have values less than 0.5.

p0050 Although the ABI is often useful in the diagnosis and determination of the severity of PAD, it has major shortcomings [22]. The presence of distal emboli, microemboli, and atherosclerotic plaques in the foot can lead to tissue breakdown, ulceration, and amputation, even if the ABI is close to 1. Furthermore, falsely elevated ABI readings occur in patients with medial wall calcification, a condition commonly seen in patients with diabetes and renal insufficiency. In these cases, the ABI reflects the ability of the vessel wall to resist compression rather than being a true indicator of the blood flow and pressure within the vessel. Consequently a recent study [22] involving diabetic patients with neuropathy showed that ABI's inability to detect arterial disease resulted in false-

356 NEUROPHOTONICS AND BIOMEDICAL SPECTROSCOPY

negative results in one-third of the limbs. Consequently, physicians often do not employ this test in diabetic patients.

p0055 Imaging methods are usually used as second-line diagnostic tests, to confirm initial diagnostic results, and to assess for a potential surgical intervention [23]. Typically, lower limb duplex ultrasound (DUS) examinations are initially performed first to determine the location of stenosis or occlusions in the legs. If this examination is inconclusive (e.g., DUS fails to visualize up to 15% of arterial segments in the calf), computed tomography angiography (CTA) is employed to provide further details of the location and extent of arterial stenoses or occlusion in the leg. However, CTA uses a potentially nephrotoxic contrast agent which thus imposes the risk of renal failure and is contraindicated in patients with renal insufficiency, a common concern in the diabetic population [24]. In addition, the use of ionizing radiation prevents CTA from being used as screening or monitoring modality.

p0060 The use of ionizing radiation can be avoided by performing magnetic resonance angiography (MRA). However, since in this case another nephrotoxic contrast agent is used (gadolinium), concerns in diabetic patients as well as those with renal insufficiency remain. MRA of small vessels in particular is often not adequate for diagnosis and treatment planning. While MRA provides details of the blood circulation in the upper and lower limb, direct information about perfusion in the foot is not provided.

p0065 Intravascular imaging techniques such as intravascular ultrasound (IVUS) and optical coherence tomography (OCT) are useful in identifying hardened plaque formations that could rupture and can cause pulmonary embolisms, strokes, and myocardial infarctions [25]. However, the application of these techniques is limited to large arteries, and neither IVUS nor OCT informs about the distal foot perfusion. Furthermore, unlike diffuse optical tomography (DOT), these methods are invasive.

p0070 Optical imaging techniques can noninvasively measure blood in tissue without the need for contrast agents or ionizing radiation. To date, promising initial results have been shown using near-infrared spectroscopy (NIRS) to detect PAD [26,27]. However, in NIRS, measurements are performed in a reflection-based geometry at isolated points on the surface of the tissue, which makes the technique heavily dependent on the location of the probe. In addition, unlike optical tomographic imaging, NIRS does not provide the physician with an image of the blood flow, but simply a time trace of the hemoglobin concentrations.

p0075 In DOT, red and near-infrared light ($650 \text{ nm} < \lambda < 900 \text{ nm}$) are used to probe biological tissues. This low-energy electromagnetic radiation ($\sim 1\text{--}2.5 \text{ eV}$) is delivered to one or more locations on the surface of the body part under investigation and transmitted and/or back-reflected light intensities are measured at distances up to 10 cm [28]. As the near-infrared light passes through tissue, it is both scattered and absorbed by a multitude of chromophores inside the tissue. Of special interest are the blood constituents HbO_2 and Hb , which have distinctly different absorption spectra in the visible and near-infrared wavelengths. By performing measurements at multiple wavelengths, concentration of these chromophores as well as derived parameters such as total hemoglobin $\text{HbT} = \text{HbO}_2 + \text{Hb}$ can be obtained [28,29]. By gathering data at different wavelengths and using multiwavelength image reconstruction codes, 2- and 3-dimensional maps of these and other parameters, such as blood volume, can be generated. With

instrumentation [12,30–32] geared specifically to the fast data acquisition rates required for dynamic imaging, this technique has increasingly been applied to other clinically relevant areas, such as breast imaging [12,32], arthritis detection [14], and cancer research in small animals.

p0080 Even when the existing modalities (ABI, DUT, CTA, MRA) are used in combination, there are considerable gaps in the diagnosis of PAD, largely due to the fact that all of these modalities are surrogate measurements of distal perfusion. Since it is the lack of distal perfusion that leads to ulcers and amputations, a direct measure of this perfusion is necessary. Dynamic vascular optical tomographic imaging (VOTI) promises to overcome the limitations of current diagnostic techniques and could become a platform for assessing various vascular diseases. It has the capability to image the temporal response of the vasculature to an external provocation and use this response as a diagnostic marker. In addition, optical imaging systems use less expensive parts than most other imaging instrumentation and can be scaled down to portable systems. Therefore, optical imaging systems could be used at point of care as readily available screening devices and has the potential to be a safe and accurate method to diagnose PAD and allow for monitoring of treatment response.

s0025 2.2 Methods

s0030 2.2.1 Study Population

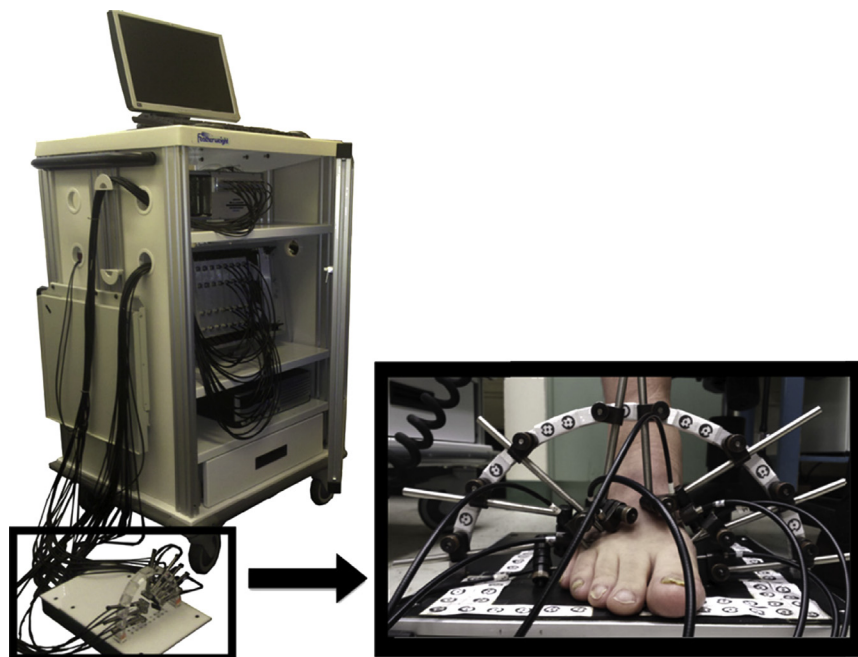
p0085 Forty subjects were recruited for this institutional review board (IRB)–approved diagnostic pilot study in the Division of Vascular Surgery at New York Presbyterian Hospital—Columbia University. The IRB of the NYP approved the human subject protocol, and written consents were obtained from all patients. The patients were placed into three cohorts: healthy subjects ($N = 20$), PAD patients without diabetes ($N = 10$), and PAD patients with diabetes ($N = 10$). The physicians assigned the patients in one of the three cohorts based on a combination of the patients' ABI readings, segmental ultrasound waveforms, physical symptoms, and medical history.

p0090 The patients recruited were 75% male and 25% female, with a mean age of 67.5 ± 11.5 years. Of the patients recruited 10% were current smokers, and 20% had been smokers in the past. The ethnic makeup was 55% Hispanic, 25% non-Hispanic white, 10% African American, and 10% Asian American. Of the healthy subjects recruited none were smokers or had smoked habitually in the past. The healthy subjects were 80% male and 20% female, with a mean age of 35.6 ± 10.0 years. The ethnic makeup was 5% Hispanic, 60% non-Hispanic white, 5% African American, and 30% Asian American.

s0035 2.2.2 Instrumentation

p0100 Optical transmission measurements on the foot were performed with a digital, dynamic near-infrared optical tomography imager [31]. The VOTI system illuminates the tissue with an optical beam consisting of two laser diodes (wavelengths $\lambda = 765$ and 830 nm). The diodes are sequentially coupled into different 1 mm multimode fiber bundles that distribute light to multiple areas along the foot (Fig. 14.1). The current of each laser diode is modulated to a distinct amplitude and frequency (5–7 kHz). In this way, multiple wavelengths may be illuminated simultaneously, thereby increasing the imaging speed

358 NEUROPHOTONICS AND BIOMEDICAL SPECTROSCOPY



f0010

FIGURE 14.1 Dynamic diffuse optical tomography system and the measurement probe.

and their respective contribution to the attenuated detected signal can be extracted using synchronous detection techniques [33]. The light is attenuated and scattered as it propagates through the foot and is collected by the various detector fiber bundles positioned around the foot.

p0105 The measuring probe was designed to accommodate the various shapes and sizes of feet seen in a clinical setting. Utilizing a sandal-shaped design, optical fibers are guided toward the foot via spring-loaded shoulder screws. The probe contains 14 sources and 20 detectors placed in a two-ring arrangement. This design gives each fiber the ability to translate different lengths to make contact with the nonuniform curvature of the foot. To obtain the mesh for the image reconstruction, a photograph is taken of the patient's foot such as shown in Fig. 14.1; using two references a coordinate system can be made to identify the locations, the sources and detectors, and the segment the foot boundary.

s0040 2.2.3 Image Reconstruction

p0110 The detector readings were filtered by using the discrete cosine transform (DCT) for noise suppression and elimination of artifacts due to movement or respiration. A DCT expresses a sequence of finite data points in terms of a sum of cosine functions oscillating at different frequencies. It relates to the Fourier transform but uses only real valued coefficients [34]. The coefficients that yielded a high correlation with the original signal were used to represent the image, which enabled the feature-preserving noise reduction without the loss of curvature within the original shape. These preprocessed data were then inputted to the image reconstruction code.

p0115 To generate the two-dimensional reconstructions of the optical properties in the foot, a ~~diffusion theory-based~~ partial-differential-equation (PDE)-constrained multispectral image reconstruction scheme was employed [12]. This method solves the forward problem (boundary radiance at each wavelength) and the inverse problem (spatial distribution of chromophores concentrations) simultaneously using a reduced Hessian sequential quadratic programming (rSQP) method [12,35]. This scheme directly reconstructs the spatial distributions of the HbO₂ and Hb concentrations in the foot. Note that the differences in [HbO₂] and [Hb] obtained through reconstruction is relative to baseline which is assumed to be given by [HbO₂] = 23.43 μM and [Hb] = 14.69 μM, throughout the foot. A radial basis function (RBF)-type regularization scheme is employed to obtain quality images by reducing image noise such as artifacts near the foot surface. More details about this code can be found in reference [35]. Given source-detector configuration, and the geometry and optical properties of feet in the wavelength region considered, we expect spatial resolution of approximately ~0.5 cm in the center of the feet, and ~0.2 cm toward the surface regions [37,38].

s0045 2.2.4 *Measurement Protocol*

p0120 During the imaging protocol the subjects were asked to place their foot on the patient interface (Fig. 14.1) while sitting upright in a chair. A total of 34 fibers (14 source and 20 detection fibers) encompassed the foot, forming a coronal cross-section at the mid-metatarsal level. This location was chosen because it contains the two major arteries of the foot the dorsalis pedis and the major branches of the posterior tibial artery. Physicians often probe these arteries when measuring a patient's ABI. Furthermore, it is a common location for diabetic foot ulcers to occur and the vasculature in that region is too small to diagnose even with the high-resolution anatomical imaging modalities such as CTA and MRA.

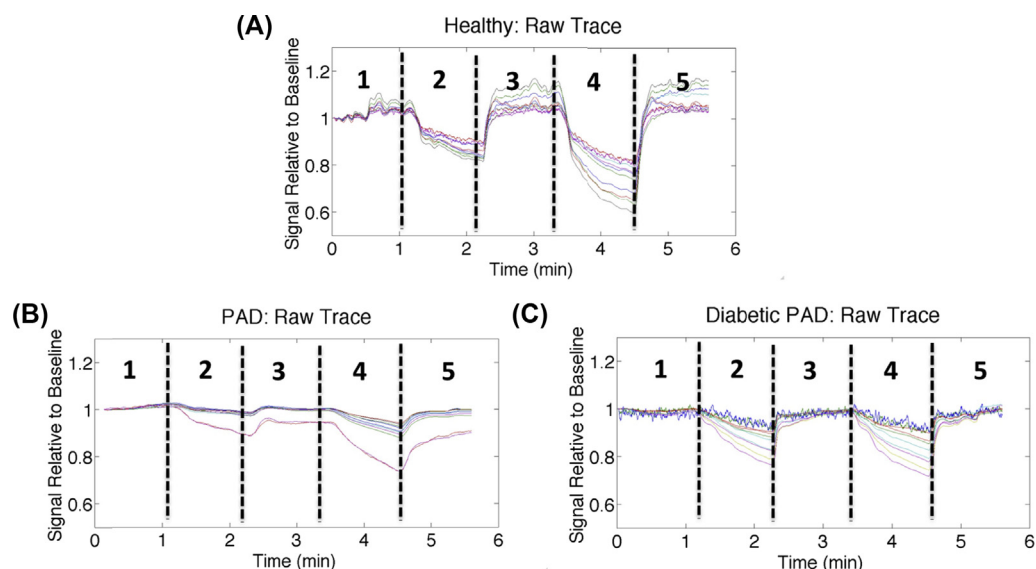
p0125 After positioning the probe around the patient's foot, the instrument automatically determined and stored the ideal gain settings for each channel at every source position. To illicit a controlled vascular response, a pressure cuff was applied to the upper thigh. Patients are familiar with leg cuffs from ABI measurements, making this dynamic protocol a natural extension of the existing diagnostic procedures. The protocol consists of five stages: First a baseline measurement was taken while the patient was seated at rest for approximately 1 min. In the second stage, a pressure cuff was inflated to 60 mmHg around the thigh. This induces venous occlusion, allowing arteries to supply blood to the foot but preventing the veins from returning it to the heart, causing the blood to pool in the foot. The pressure was maintained for 1 min after which it was rapidly released. During the third stage of the sequence, the foot was left to recover for 1 min. In the fourth portion of this protocol, a 120 mmHg was applied to the thigh inducing greater venous occlusion for 1 min. Then the pressure was released leaving the foot to recover. This five stage protocol was applied three times for each subject to show repeatability.

s0050 2.3 Results and Discussion

s0055 2.3.1 Light Intensity Time Traces

p0130 We start by presenting three select cases, one patient with PAD (ABI = 0.66), one patient with diabetes and PAD (ABI = 1.07), and one healthy subject (ABI = 1.00). Using the traditional ABI measurement, it is possible to discern between the healthy control and the PAD patient; however, the diabetic PAD patient is not distinguishable. Diabetic patients often have incompressible arteries due to calcifications which result in elevated ABI readings and leads to false-negative diagnoses.

p0135 Fig. 14.2A–C show the representative time traces for the healthy, PAD, and diabetic PAD subjects, respectively. The detector readings shown are normalized to the first 30 s of the initial rest period. The time traces have five distinct phases that correlate with the measurement protocol shown in Fig. 14.2. Initially, we see a flat segment in concordance with the rest period. Subsequently a drop in intensity occurs, upon applying the 60 mmHg thigh cuff inducing venous occlusion. During venous occlusion, blood is pumping from the arteries into the foot but not returning to the heart, it pools in the foot. The greater blood volume in the foot increases the light attenuation resulting in the drop of signal observed during the venous occlusion stages of the measurement protocol.



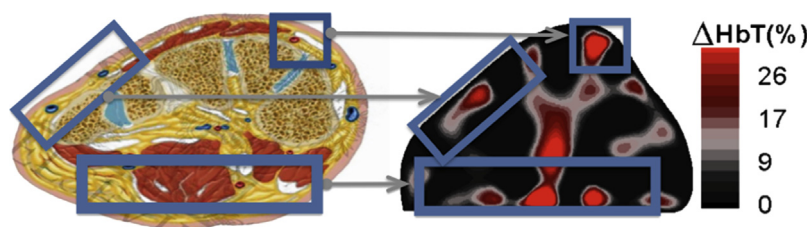
f0015 **FIGURE 14.2** Normalized detector readings (different detector positions shown as colored lines (grey in print versions)) for a single-source illumination over time for (A) a healthy volunteer, (B) peripheral artery disease (PAD) patient, and (C) a diabetic PAD patient. The individual traces were filtered with a 50-point moving average filter. A dip in intensity is observed at approximately 1 min when the 60 mmHg cuff is applied to thigh. This impedes blood from returning to the heart and causes it to pool in the leg increasing light absorption. Upon release of the cuff, the signal returns to baseline; the same behavior can be seen with the 120 mmHg cuff. There are clear differences in the magnitude drop during thigh occlusions as well as the recovery rates from release of the thigh cuff.

After 1 min of occlusion the thigh cuff is released enabling the blood to flow back to the heart and the signal to return to baseline. A 120 mmHg is applied again to the thigh inducing greater blood pooling and a greater drop in detector intensity for about 1 min before release allowing the signal to return once again to rest.

p0140 During both the 60 and 120 mmHg occlusions the healthy volunteer had a significantly greater percent drop in detector intensity (20% and 45%) than the PAD patient (10% and 15%) and the diabetic PAD Patient (20% and 20%). These amplitude drops were calculated by observing the largest magnitude change among the different detectors for the same source position before the release of the 60 and 120 mmHg pressure occlusions. The detector readings reflect the amount of light that passes through the tissue. The more blood present in the tissue, the less light is transmitted. As a result, the signal attenuation is directly proportional to the total hemoglobin concentration this implies that more blood collects in the foot during occlusion in the healthy subject than in the patients with affected vasculature. Furthermore, the decay and recovery rates of the detector intensities differ between the three subjects. The healthy volunteer exhibits a fast decay in the detector intensity and the occlusion rate has a distinct plateau phase while the PAD patients exhibit a more linear trend. It is suspected that the PAD patients exhibit a more linear trend because the diseased arteries provide greater flow resistance due to plaque buildup and a lack of arterial wall capacitance due to arterial wall calcifications. Despite the similarity in the ABI measurements of the diabetic PAD patient and the healthy volunteer, VOTI detector readings provide contrast between the two subjects providing useful information that is missing within the current diagnostic methods.

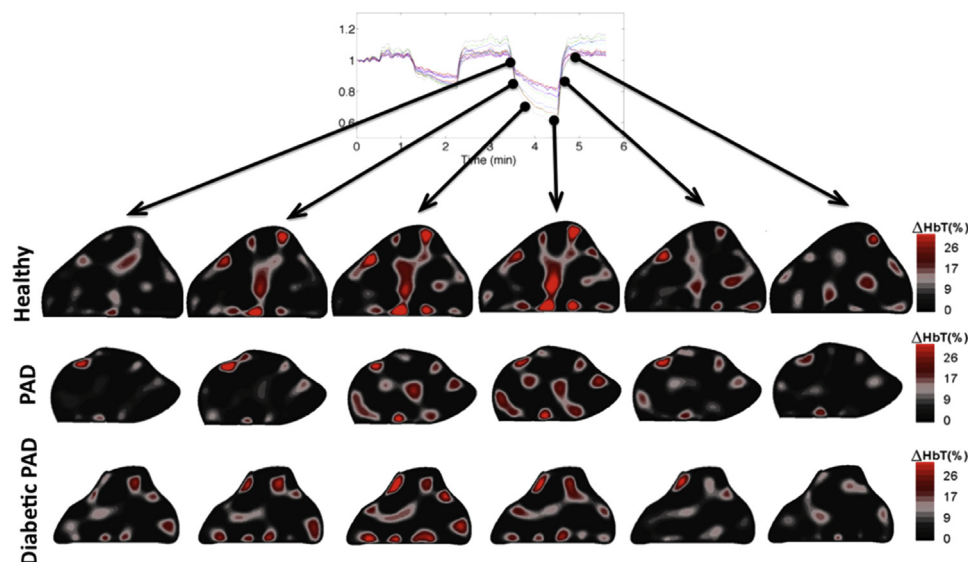
s0060 2.3.2 *Image Reconstructions*

p0145 The detector readings from multiple source positions were used to reconstruct a two-dimensional cross-sectional image of the change in total hemoglobin concentration [HbT] within the foot. These reconstructions appear to coincide spatially with the expected foot vasculature. Fig. 14.3 shows a side-by-side comparison between an anatomical cross-section adapted from an anatomy textbook and a healthy foot reconstruction image. The changes in hemoglobin concentration occur in the periphery of the foot as expected anatomically, which could enable physicians to evaluate spatial foot perfusion.



f0020 **FIGURE 14.3** The locations of hemoglobin change within the 2D reconstructions correlate with the expected anatomy of the cross-section of the foot.

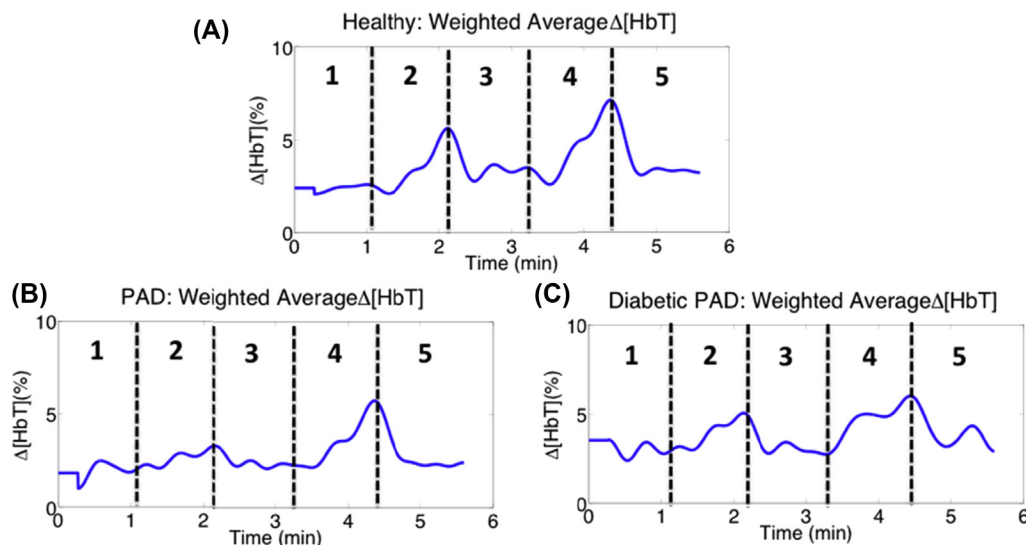
362 NEUROPHOTONICS AND BIOMEDICAL SPECTROSCOPY



f0025 **FIGURE 14.4** Dynamic changes occurring during the 120 mmHg occlusion within the cross-section of the foot along the course of the imaging sequence. There appears to be a faster reaction to the thigh cuff within the healthy foot than the feet with the affected vasculature as well as a greater change in the total hemoglobin concentration.

p0150 **Fig. 14.4** shows the image reconstructions at six time points during the 120 mmHg thigh cuff occlusion. In these images we can see the hemoglobin concentration gradually increasing within the foot during the occlusion portion of the imaging sequence and then decreasing back to baseline upon removal of the pressure cuff. The healthy subject, PAD patient and the diabetic PAD patient exhibit different time courses with respect to both intensity and rate of change of the hemoglobin concentration. The healthy subject has the largest magnitude transition from the beginning of the occlusion to right before the cuff removal at the fourth time point. Furthermore, the amount of blood in the foot made a full recovery back to resting state. The PAD patient exhibits a slower rate and magnitude of blood pooling before the release of the thigh cuff than the healthy patient. This is expected due to the effects of plaque accumulation in the arteries impeding the blood flow. The diabetic PAD patient had a slower rate and the dynamics were not nearly as apparent. The initial change in concentration of hemoglobin within the foot was relatively high before the 120 mmHg occlusion; this is most likely due to an incomplete recovery from the previous 60 mmHg occlusion. Physiologically the incomplete recovery can be caused by obstructions of the capillary bed of the foot. We suspect that these microvasculature occlusions may cause the blood to remain in the foot and not flow to the veins during the 60 mmHg occlusion leading to a higher starting concentration for the subsequent occlusion.

p0155 Looking at the blood volume dynamics within the foot, we see that the two time points prior to release of the thigh cuffs show the most significant differences between



f0030 **FIGURE 14.5** Area weighted average total hemoglobin signal for (A) healthy volunteer, (B) a peripheral artery disease (PAD) patient, and (C) a diabetic PAD patient. We recover the five phases seen in the raw detector time traces and observe more blood pooling within the healthy volunteer than the patients with affected vasculature.

the three cases. These images show clear differences between the healthy patient and the two PAD patients. We observe that the changes in [HbT] are much less pronounced in the feet of the PAD patients than the healthy volunteer. This suggests that there is significantly less blood pooling in PAD patients' feet during a minute of venous occlusion. Physiologically we suspect that the differential is due to the blood flow impedance caused by plaque in the affected vasculature as well as arterial stiffening due to calcifications within the arterial wall lowering the vascular compliance.

p0160 To further quantify the hemodynamic change within the feet we calculated the sum of the [HbT] in each frame of the dynamic imaging sequence and obtained an area weighted average signal (Fig. 14.5). These time traces show that the amount of blood within the foot increased when the thigh cuff was applied to the foot (phases 2 and 4 in all images in Fig. 14.5). The concentration of hemoglobin in the foot during thigh occlusions is greatest within the healthy volunteer (Fig. 14.5A), in concordance with the time-dependent detector readings. Furthermore, the patients with diseased vasculature (Fig. 14.5B and C) show slower occlusion and recovery rates than the healthy volunteer.

s0065 2.3.3 Regions of Hemodynamic Consistency

p0165 To better quantify which regions in the foot contribute most to the area weighted average changes, we calculated the cross-correlation coefficients between the area weighted average change in [HbT] over the whole cross-section (see Fig. 14.5) and

364 NEUROPHOTONICS AND BIOMEDICAL SPECTROSCOPY

the change in [HbT] for each pixel within the cross-section over time using the following equation:

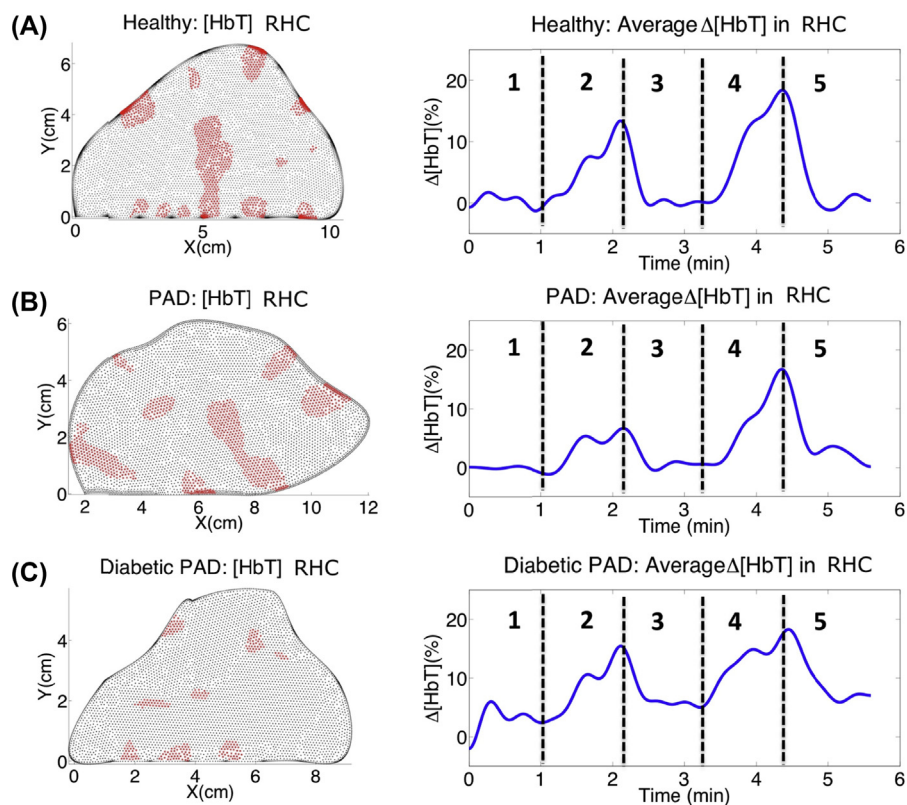
$$\rho = \frac{\sum_{t=0}^{N-1} (h(t) - \mu_h) * (W(t) - \mu_w)}{\sum_{t=0}^{N-1} \sqrt{(h(t) - \mu_h)^2} * \sum_{t=0}^{N-1} \sqrt{(W(t) - \mu_w)^2}} \quad (14.1)$$

where $h(t)$ is an individual pixel time trace from within the foot and $W(t)$ is the weighted average signal from the entire foot (both time series are of length N .) The pixels that contribute the most to the area weighted average change (here defined as $\rho > 0.7$) are plotted in red in Fig. 14.6. These regions of hemodynamic consistency (RHC) show the spatial locations that correspond to the vascular response, eliminating potential artifacts and background noise. By counting all pixels with $\rho > 0.7$, we find that a healthy subject and the PAD patient both have 22.5% of their pixels correlating to the weighted average signal, while the diabetic PAD has only 6.18% of its pixels correlating with the weighted average signal. This suggests there is a severe difference in the hemodynamics of diabetic patient's vasculature.

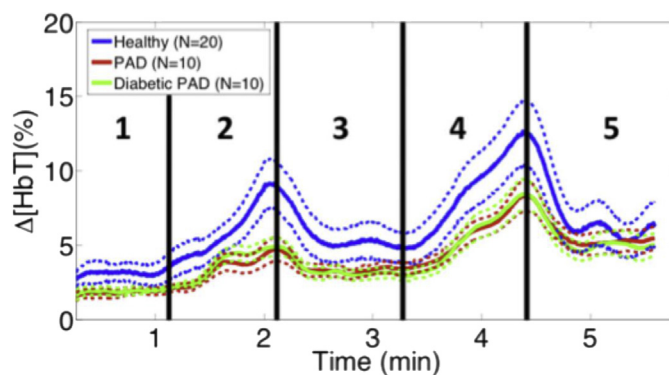
p0170 Taking the weighted average signal within the RHC shown in red we obtain the adjacent time traces in Fig. 14.6. The signals from within the RHC show cleaner signals for the three different cases; these signals coincide more with the vasculature of the foot and are less adulterated by noise and artifacts. The healthy volunteer shows the highest concentration of blood pooling during the occlusions and has a significantly faster occlusion and decay rate. Within the RHC the PAD patient exhibits a lower concentration of hemoglobin during the occlusions but has a slower occlusion and decay rate than seen in the weighted average total hemoglobin signal within the whole foot. The diabetic PAD patient has the lowest concentration of hemoglobin change, and the concentration of hemoglobin does not return fully to rest within the 1-min recovery time of the imaging sequence.

s0070 2.3.4 Cohort Time Traces

p0175 Going beyond the three case studies and to look at difference between the three cohorts (healthy volunteers, diabetic PAD patients, and nondiabetic PAD patients), we averaged the hemoglobin time traces for each of the three cohorts. The results are shown in (Fig. 14.7). The standard error bars for the healthy cohort do not overlap with those of the patient cohorts. The hemoglobin change before release of the 60 mmHg occlusion for the healthy subjects is almost double that of the patient cohorts ($\sim 10\%$ vs. 5%), showing the greatest discrepancy between the cohorts. Furthermore, the hemoglobin time traces for the PAD and the diabetic PAD cohorts are very similar unlike their ABI readings. The PAD patient cohort had an average ABI of 0.64 ± 0.21 indicating moderate disease, while the diabetic PAD cohort had an average ABI of 0.95 ± 0.35 , which would be misinterpreted as healthy vasculature. A statistical significance ($P = .05$) is observed between the ABI readings despite both cohorts being diagnosed with PAD by the physician. This is due to arterial calcifications, which render the arteries of incompressible and falsely elevate the ABI readings.



f0035 **FIGURE 14.6** Pixels that correlate with weighted average total hemoglobin signal and their corresponding time traces for (A) a healthy volunteer, (B) a peripheral artery disease (PAD) patient, and (C) a diabetic PAD patient. By using regions of hemodynamic consistency (RHC) we see much cleaner signals than the weighted average signals and the differences in the vascular dynamics become much more apparent.



f0040 **FIGURE 14.7** This figure shows the cohort average signals with their standard error bars. The healthy cohort average's error bars rarely overlap with those of the peripheral artery disease (PAD) cohorts. Furthermore, the biggest discrepancy occurs before release of the 60 mmHg occlusion. There is little difference between the PAD and diabetic PAD cohorts, suggesting that VOTI is unaffected by arterial compressibility.

366 NEUROPHOTONICS AND BIOMEDICAL SPECTROSCOPY

s0075 2.3.5 Diagnosis Using the 60 mmHg Occlusion Peak

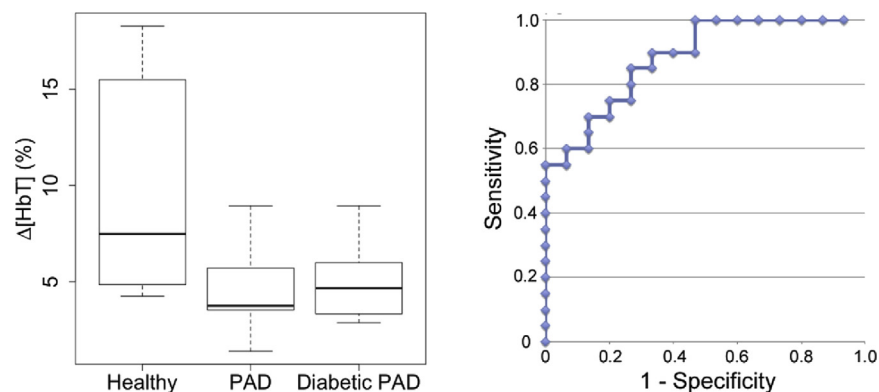
p0180 We extracted the 60 mmHg occlusion peak and created boxplots for each cohort (Fig. 14.8). The boxplots show the median of the healthy subjects is almost double that of the PAD and diabetic PAD subjects (7.5%, 3.8%, and 4.5%, respectively). The largest change within the healthy cohort is 18.27%, while the PAD cohorts have a maximum of less than 9% change. The range of the healthy cohort is greater than the PAD and diabetic PAD cohorts (14.0%, 7.5%, 6.1%).

p0185 The healthy cohort had a mean of 9.84 ± 5.44 (%), the PAD cohort had a mean of 4.41 ± 2.02 (%), and the diabetic PAD cohort had a mean of 4.78 ± 1.93 (%). Applying a one-way analysis of variance (ANOVA) a between-group P -value of .003 was obtained. Using the Holm t -test, the healthy cohort showed a statistical significance from both PAD cohorts while the PAD and diabetic PAD cohorts were not different from each other ($P = .006$, $P = .006$, $P = .34$).

p0190 A receiver operating characteristic (ROC) curve was derived using the 60 mmHg peak for diagnosis (Fig. 14.8). This is a good classifier for PAD with an area under the ROC curve (AUC) of 0.81. Designating $\Delta[\text{HbT}] < 6.1\%$ as afflicted, we achieve a sensitivity (Se) of 0.85 and specificity (Sp) of 0.73. The positive predictive value (PPV) is 0.81, and the accuracy of the test equals 0.80. If higher specificities are desired, the cutoff can be lowered to 5.0%, achieving an Sp of 0.87 and Se of 0.70. The PPV is 0.88, and the accuracy of the test equals 0.77.

s0080 2.4 Discussion

p0195 VOTI is a noninvasive, nonionizing, contrast-free imaging modality that uses harmless red and near-infrared light to measure changes in hemoglobin concentrations in tissue.



f0045 **FIGURE 14.8** (Left) These boxplots show the distribution of $\Delta[\text{HbT}]$ at the end of the 60 mmHg occlusion for each cohort. The healthy cohort has a greater minimum, maximum, and quartiles than the affected cohorts, signifying more pooling in the leg. The healthy cohort has a larger range, which may be caused by lifestyle choices or asymptomatic circulatory problems. Also, note the affected cohorts have similar distributions despite arterial calcifications. (Right) This figure shows an ROC curve created using the $\Delta[\text{HbT}]$ before release of the 60 mmHg thigh cuff occlusion. This is a good classifier with an AUC of 0.81. Designating $\Delta[\text{HbT}] < 6.1\%$ as afflicted, a sensitivity of 85% and a specificity of 73% were achieved.

This technology has been applied to image PAD in the foot. VOTI shows a statistically significant difference between the hemoglobin changes in healthy and affected vasculature in the foot. There is more blood pooling resulting in high total hemoglobin concentration in the foot during a 1-min 60 mmHg venous occlusion in healthy subjects than in the PAD and the diabetic PAD cohort ($P = .006$, $P = .006$). For large vessel disease, the plaque buildup increases the resistance and reduces compliance of the vessels. This leads to a reduction in the blood pooling into the foot, resulting in lower total hemoglobin concentrations. In small vessel disease, the same effect can be caused by arterial stenosis. This analysis was also completed for 120 mmHg occlusion, which was not as effective. We suspect this is due to 120 mmHg causing partial arterial occlusion in patients with lower blood pressure.

- p0200 Diagnostic parameters can be extracted to form a decision boundary to diagnose PAD in the lower extremities. The maximum hemoglobin concentration from the 60 mmHg thigh cuff occlusion was used to classify the disease. Assessing the distribution, we found considerable differences in the boxplots showing greater pooling the median and quartile values within the healthy subjects. A greater range was observed however for the healthy individuals which may be caused by lifestyle choices (e.g., diet, smoking) or other medical conditions.
- p0205 Using ROC curve analysis we found the 60 mmHg peak to be a good classifier of PAD with an AUC of 0.81. Using a $\Delta[\text{HbT}] < 6.1\%$ as the decision boundary, VOTI obtained an $\text{Se} = 0.85$ with $\text{Sp} = .73$. A lower cutoff $\Delta[\text{HbT}] < 5.0\%$ yields an $\text{Sp} = .87$ but lowers Se to 0.70. Varying the cutoff $\Delta[\text{HbT}]$ enables the user to choose whether sensitivity or specificity is more important in their clinical decision-making.
- p0210 These results indicate that a physician can effectively diagnose patients with PAD independently of arterial calcifications using the VOTI system, despite the ABI measurements not being accurate. In addition, the parameters extracted from the VOTI images correlate fairly well ($R^2 = 0.84$) with the ABI readings for the nondiabetic PAD patients. We also observed greater $\Delta[\text{HbT}]$ in the healthy subjects than the subjects with mildly, moderately, and severely diminished foot PVR waveforms ($P = .04$, $P = .003$, $P = .0007$). The results showed greater $\Delta[\text{HbT}]$ in the mildly diminished than the subjects with moderately and severely diminished waveforms. This suggests that it is not only a decision boundary, but can identify the severity of the disease. In addition, VOTI's ability to noninvasively provide localized physiological information can greatly aid in the assessment of neuroischemic ulcers in diabetic PAD patients and help with over/undertreatment of arterial disease. Angiosome analysis using the VOTI system may aid in treatment planning, where a physician can intervene to improve perfusion to the most compromised areas of the foot. There is currently no gold standard for assessing angiosome perfusion making statistical analysis difficult. Future studies involving animal models or angiographic analysis of the foot in patients with distal arterial disease may help to validate angiosome analysis using VOTI.
- p0215 Unlike the traditional diagnostic modalities, VOTI provides a direct measurement of the perfusion in the entire foot, serving as an end-stage measure of the effects of the

368 NEUROPHOTONICS AND BIOMEDICAL SPECTROSCOPY

lesions or stenosis on the foot. This technology can be used to noninvasively diagnose as well as monitor patients with PAD independent of arterial calcification, without the need to inject contrast agents into the patient's blood stream.

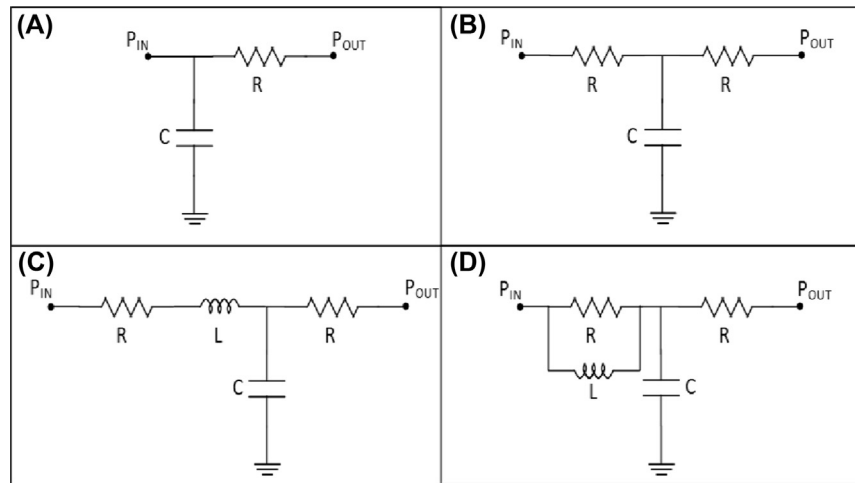
s0085 2.5 Modeling of Blood Flow

s0090 2.5.1 Background

p0220 To further improve the results obtained and to better understand the underlying physiological factors that could explain the observed hemodynamic effects, we have developed a computational model of the vascular system under consideration. A first representation of the large vessels system with an "air chamber" (in German "Windkessel") of a fire engine was developed by Otto Frank in the late 19th century [39,40]. He argued that the elasticity of the arterial wall and that of the air in the Windkessel lead to analogous phenomena and hence simulated the behavior of the heart using a closed hydraulic system with a high pressure (systolic) and low pressure (diastolic) states (see also Ref. [41]). During the second half of the 20th and the beginning of the 21st century, the simplified one-dimensional form of the fluid dynamics Navier–Stokes equation was used to describe the time-dependent blood flow in a straight rigid vessel and, as boundary conditions, Windkessel models (also called zero-dimensional or lumped models) were then derived from electrical circuit analogies (RCL circuits), instead of air chambers in fire engines [41–45]. The main advantages of these models are that they rely on simple first-order differential equations [44,45], reduce the number of parameters to consider [46], and can be easily related to physiological parameters. Therefore, these models are relatively easy to solve and help to understand the global distribution of pressure, flow, and blood volume under various physical conditions [46–48]. For example, one of the early successes using RCL models was the realization that the compliance corresponds to the elasticity of the vessel and that the resistance is inversely proportional to the blood vessel radius to the fourth power following Poiseuille law [42,46–49].

p0225 Initially, only the behavior of the arterial tree was considered and usually the lumped models were used as boundary conditions for the Navier–Stokes equations [46,47]. Three different RCL vascular models (which in literature are still often called "Windkessel" models for historical reasons) were typically used: the two-elements model comprising only a single resistor and capacitance, the three-elements model, in which a second resistor was added, and the four-elements model, in which also an inductance was added in series or parallel to the first resistor to represent fast effects in the blood behavior (Fig. 14.9).

p0230 To study wave transmission phenomena, these simple models were refined by introducing modular models [41,45,46,48,49] that allowed to compartmentalize the vascular tree. With these changes, closed loops in the circulations [41,48,49] could be modeled and the characteristics of the venous return could be considered by adding in series or parallel basic lumped-parameters compartments, each characterized by its



f0050 **FIGURE 14.9** (A) represents the two-elements Windkessel model; (B) represents the three-elements Windkessel model; (C and D) are two possible variations present in literature for the four-element Windkessel model.

resistance, capacitance, and inductance [45,46,48]. The artery, arteriole, capillary, and veins are then represented with different values and components. The main arteries are very elastic, and the blood flow is pulsatile. Therefore, these arteries display all typical effects related to resistance, compliance, and inductance. In the arterioles and capillaries, the resistance dominates over the other parameters [46]. In the veins, the compliance is much higher than in the arteries [41,50] and hence the blood flow is relatively steady; therefore an RC combination is usually considered sufficient to describe hemodynamics in the vein compartment [46].

p0235 While all these models are used to examine the blood pulse in the arterial and venous system, they do not consider time-dependent, externally driven, hemodynamic changes. To address this issue, Stiukhina et al. [50] and Mashayekhi et al. [51] recently attempted to model the effects of a brachial artery cuff inflation in healthy patients. Stiukhina et al. modeled the venous system as an RC ladder. The cuff inflation was modeled by setting the blood flow (electrical current) exiting from the circuit to 0. In contrast, Mashayekhi et al. simulated the cuff effect as a variable resistor, while approximating the effect of the venous system as an ideal pressure generator. Both groups were only interested in the shape of the blood wave in the arterial tree, and the cuff inflation was a high, steep ramp (0.3 s) and held for 5 min. Both groups focused on the differences between the state before and after the cuff occlusion but did not consider the transitional hemodynamic between these two states.

p0240 The model we discuss here goes beyond previously considered approaches in several ways. Our objective was not to estimate the shape of the blood pulse, or compare two different system states but to model the time-dependent dynamic accumulation of the blood in the foot due to a cuff occlusion of the veins in the leg. Hence, we adapted the modular RC to allow for hemodynamic effects. In particular, we introduced two dynamic

370 NEUROPHOTONICS AND BIOMEDICAL SPECTROSCOPY

variable resistors to represent the cuff inflation/deflation and evaluated the changes in pressures in the various compartments during the cuff inflation/deflation. We compared the results obtained with this newly created model with the experimental clinical data previously acquired. This comparison gave us new insights into the physiological underpinnings of the observed effects, which in turn led to improved diagnostic sensitivity and specificity, as will be discussed in more detail in the results section (Section 2.5.3).

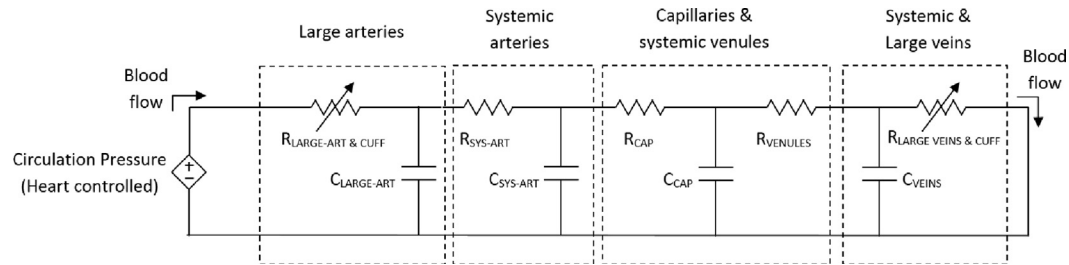
s0095 2.5.2 Formulation of the Model

p0245 To assess the dynamic accumulation of blood in the foot of healthy and PAD patients, we adopted a multicompartamental derivation of the Windkessel model [46]. In our model, each subsection of the vasculature is represented by a combination of capacitors (which represent the vessels' elasticity and compliance), resistors (which represent the resistance to the blood flow), and inductors (which represent the blood inertia). Consequently, the blood pressure and flow were modeled with a voltage and a current, respectively. To represent the relationship between the drop in pressure in each vascular compartment and the blood flow through it, we used Ohm's law ($V = R \cdot I$) and a set of first-order differential equations to represent the capacitors ($C \cdot \frac{dV}{dt} = I$) and inductors ($L \cdot \frac{dI}{dt} = V$).

p0250 Our initial studies with this model suggested that the effects of the inductors, which are used to portrait fast changes in the blood flow [49], were negligible compared to the effects of the other components. This is not surprising since we are interested in the accumulation of blood in the foot over a minute-long cuff inflation; hence fast changes (on a subsecond or second scale) in the blood flow do only play a minor role. Consequently, we simplified the model and reduced the total number of parameters present in the system. As a result, the final model we implemented consisted of four subsections: (1) large arteries; (2) systemic arteries; (3) capillary bed and systemic venules; and, (4) large veins. Each resistor was connected in series to the following resistor, whereas the capacitor was connected in parallel to the following compartments, forming a ladder circuit (Fig. 14.10).

p0255 During our clinical VOTIS measurement protocol, we used a thigh cuff to occlude the veins that carry the blood back to the heart. In particular, during a single experimental acquisition, two consecutive 1-min cuff inflations were applied, separated by a 1-min interval between them [17]. To simulate the inflation and deflation of the cuff, the resistances used for the main veins and arteries sections were considered variable and increasing during an inflation. This is consistent with the fact that the cuff inflation causes a reduction of the blood flow through the blood vessel at the cuff location and a correspondent increment in the pressure before that location. After the deflation, this pressure decreases again to the resting-phase value.

p0260 The cuff was operated manually, thus maximum pressures of 60 and 120 mmHg were not obtained immediately. To model this effect, we explored linear and exponential functions to simulate the increasing/decreasing values for the resistances. We found that exponential fits provided a better match with the data.



f0055

FIGURE 14.10 Schematic of the model implemented.

p0265 Furthermore, we considered the possibility of a partial delayed arterial occlusion. It is well known that in a cuff experiment, veins are compressed before arteries become compressed. We, therefore, employed a delay parameter that is accounting for this fact in our simulations.

p0270 The following system of four first-order differential equations was thus obtained:

$$\left\{ \begin{array}{l} \frac{dV_{CL}}{dt} = -\left(\frac{1}{C_{LA}R_{LA}(t)} + \frac{1}{C_{LA}R_{SA}}\right) \cdot V_{CL} + \frac{1}{C_{LA}R_{SA}} \cdot V_{CS} + \frac{V_{Heart}(t)}{C_{LA}R_{LA}(t)} \\ \frac{dV_{CS}}{dt} = \frac{1}{C_{SA}R_{SA}} \cdot V_{CL} - \left(\frac{1}{C_{SA}R_{SA}} + \frac{1}{C_{SA}R_C}\right) \cdot V_{CS} + \frac{1}{C_{SA}R_C} \cdot V_{CC} \\ \frac{dV_{CC}}{dt} = \frac{1}{C_C R_C} \cdot V_{CS} - \left(\frac{1}{C_C R_C} + \frac{1}{C_P R_{VEN}}\right) \cdot V_{CC} + \frac{1}{C_C R_V} \cdot V_{CV} \\ \frac{dV_{CV}}{dt} = \frac{1}{C_V R_V} \cdot V_{CC} - \left(\frac{1}{C_V R_V} + \frac{1}{C_V R_V(t)}\right) \cdot V_{CV} \end{array} \right. \quad (14.2)$$

where,

$$R_V(t) = R_V(0) + R_{CUFF-V}(t) \quad (14.3)$$

$$R_{CUFF-V}(t) = \begin{cases} 0 & t_{start} \rightarrow t_{start_infl} \\ \exp func \ 0 \rightarrow R_{CUFF-V} & t_{start_infl} \rightarrow t_{end_infl} \\ R_{CUFF-V} & t_{end_infl} \rightarrow t_{start_defl} \\ \exp func \ R_{CUFF-V} \rightarrow 0 & t_{start_defl} \rightarrow t_{end_defl} \\ 0 & t_{end_defl} \rightarrow t_{end} \end{cases} \quad (14.4)$$

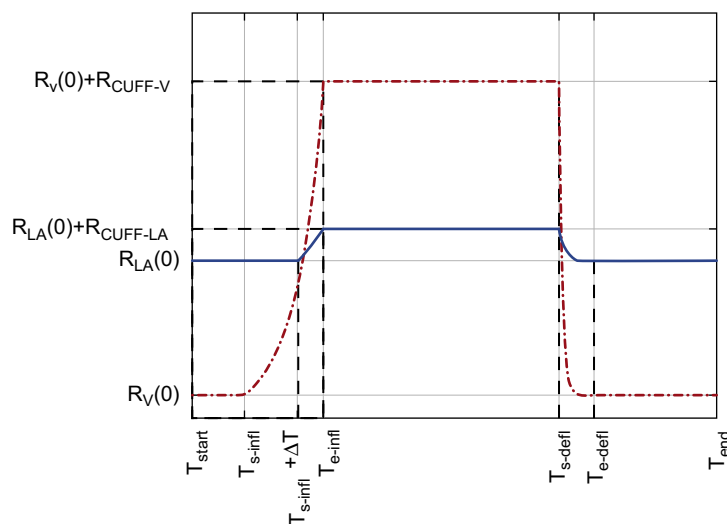
$$R_{LA}(t) = R_{LA}(0) + R_{CUFF-LA}(t) \quad (14.5)$$

$$R_{CUFF-LA}(t) = \begin{cases} 0 & t_{start} \rightarrow t_{start_infl} + \Delta t \\ \exp func \ 0 \rightarrow R_{CUFF-V} \cdot X & t_{start_infl} + \Delta t \rightarrow t_{end_infl} \\ R_{CUFF-V} \cdot X & t_{end_infl} \rightarrow t_{start_defl} \\ \exp func \ R_{CUFF-V} \cdot X \rightarrow 0 & t_{start_defl} \rightarrow t_{end_defl} \\ 0 & t_{end_defl} \rightarrow t_{end} \end{cases} \quad (14.6)$$

372 NEUROPHOTONICS AND BIOMEDICAL SPECTROSCOPY

where t_{start} is the starting time of the data collection, t_{start_infl} is the starting time for the cuff inflation, t_{end_infl} is the ending time of the cuff inflation, t_{start_defl} is the starting time for the cuff deflation, t_{end_defl} is the ending time of the cuff deflation, t_{end} is the ending time of the data collection, Δt is a delay before the arteries are affected by the cuff, and X is a multiplication factor between 0 and 1 that links the cuff effect on the veins and arteries. An example of the time-dependent functions $R_V(t)$ and $R_{LA}(t)$ is shown in Fig. 14.11.

p0275 This system of equations can be solved by employing the Euler method [48] with time step Δt smaller than the one used to characterize the heartbeat. The model was implemented and solved in MATLAB. A graphic user interface was created to facilitate the manipulation of the different parameters. The heartbeat was modeled using typical electrocardiogram and physiological pressures [41,48,52,53]: heart rate of 75 beats/min, systolic pressure of 120 mmHg, and diastolic pressure of 80 mmHg. The cuff inflation and deflation times used were set to mean values obtained from experimental tests. Overall, the total number of variables changed in the simulations was 11. This includes the five resistances (R_{LA} for the large arteries, R_{SA} for the systemic arteries, R_C for the capillaries, R_{VEN} for the systemic venules, and R_V the systemic and large veins), the four capacitances (C_{LA} for the large arteries, C_{SA} for the systemic arteries, C_C for the capillaries and venules, and C_V for the veins), and two resistance values ($R_{CUFF-V}(t)$ and $R_{CUFF-LA}(t)$) directly correlated between them, to show the effect of the cuff inflation, respectively, on the large veins and arteries.



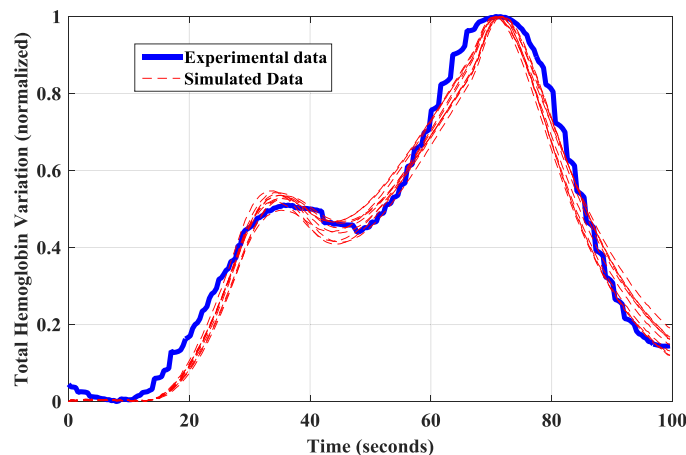
f0060 **FIGURE 14.11** Example of the time-dependent functions $R_V(t)$ (red [dark gray in print version]) and $R_{LA}(t)$ (blue [gray in print version]) for a specific combination of the simulation parameters for a cuff inflation/deflation cycle.

s0100 2.5.3 Results

p0280 An example of a typical hemodynamic response during a cuff inflation/deflation (120 mmHg) is shown in Fig. 14.12 (blue curve). Here the cuff is inflated at $t = 10$ s. Subsequently, we can see an increase in total hemoglobin for about 20 s, before a first plateau is reached. Sometimes, as in the case shown, this plateau becomes a “dip” in which the variation of total hemoglobin ($\Delta[\text{HbT}]$) briefly decreases, before a further increment is observed. In Fig. 14.12 a second maximum is reached at $t = 70$ s. At that point the cuff is deflated and $\Delta[\text{HbT}]$ returns to baseline.

p0285 To fit this curve and obtain a better understanding of the physiological underpinning, we started our analysis by varying all 11 parameters of the model over suitable physiological ranges. Theoretically, the starting values for the RC parameters could be obtained exactly from the pressure/flow data measured in the corresponding positions of the circulatory system. However, multiple different indices have been estimated in literature and no one has proven superior [43,46,54,55]. We therefore decided to avoid invasive imprecise measurements and set possible ranges for each parameter in order to obtain expected quantities of flows and pressure drops between the four sections of the model [41,46,50,52,53].

p0290 With the ranges and step sizes given in Table 14.1, we created a look-up table with about 20 million curves reflecting possible combinations of the 11 variables. From these tests, we noticed that some variables can be clearly connected to physiological effects. For instance, the presence of the plateau/dip before the maximum value in the total hemoglobin variation is strongly dependent on the cuff inflation effect on the arteries ($R_{\text{CUFF-V}}$ and X). Furthermore, the slope after the cuff is deflated seems strongly related to the veins’ resistances and capacitances (R_V and C_V).



f0065 **FIGURE 14.12** Example of a typical hemodynamic response to a cuff inflation/deflation (120 mmHg) recorded with our VOTI system (blue [gray in print version] curve). Also shown are 10 “best” fittings (red [dark gray in print version] dotted lines) obtained automatically by the program.

t0010

Table 14.1 Variables Range

Variable Name	Min Value	Step	Max Value
R_{LA}	1.5	2	9.5
R_{SA}	1.5	2	9.5
R_C	1	1	5
R_{VEN}	0.5	1	3.5
R_V	0.5	0.5	2
C_{LA}	0.1	0.4	2.1
C_{SA}	1	1	4
C_C	1	1	4
C_V	5	5	25
R_{CUFF-V}	7	3	19
X	0	0.1	0.4

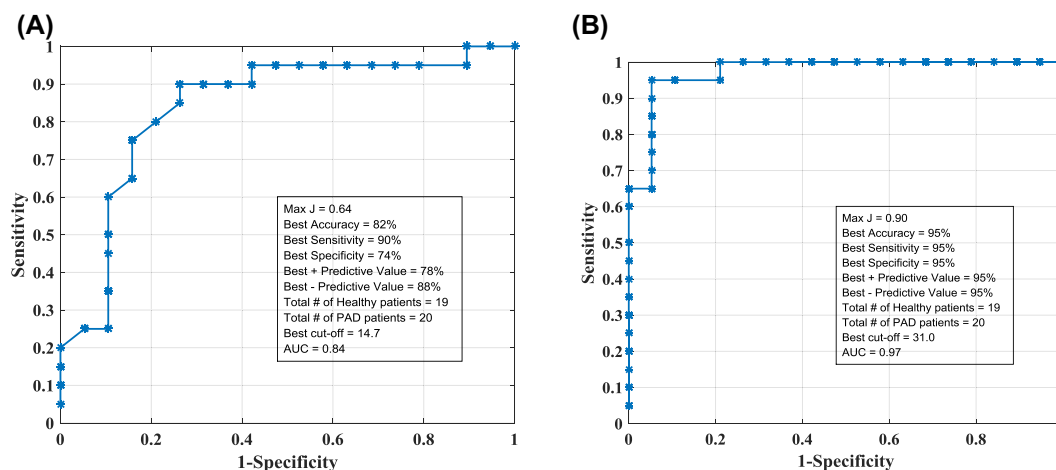
p0295 Next, we compared each inflation/deflation period of the experimental data to the simulated data. To find the simulated curves in the look-up table that best matched the experimental observations, we implemented an automatic fitting algorithm that evaluates the root mean square error between all the simulated and experimental data. To further increase the precision of the estimated values for the variables, the mean values in the 10 fittings with least root mean square error were calculated. In Fig. 14.12, the red curves show an example of the 10 best fittings.

p0300 The following step consisted in finding the parameter that best represents the differences between healthy subjects and PAD patients. Therefore, we asked, “is there any particular parameter or sets of parameters that can be used to classify a hemodynamic response as belonging to a PAD patient with high sensitivity and specificity?” Based on physiological observations, explained in the following paragraphs, we decided to focus our attention on the system’s total resistance:

$$R_T = R_{LA}(t) + R_{SA} + R_C + R_{VEN} + R_V(t) \quad (14.7)$$

p0305 As noted in the introduction to this Section, according to Poiseuille law, the resistance is inversely proportional to the blood vessel radius to the fourth power [42,46,48]. Since the plaque accumulation greatly reduces the internal diameter of arteries and veins [56], one would expect a substantial difference between healthy subjects and PAD patients, making this parameter a good choice to find differences between patients.

p0310 One could also expect that there would be a reduction in the capacitance of the arteries or the veins since the deposit of lipids, cholesterol crystals, and calcium salt reduces their compliance and the vessels cannot expand in size to accommodate more volume [56]. However, the latter phenomenon had been proved to be more difficult to estimate with a Windkessel-based model [55,56]: unlike for the resistances, the total



f0070 **FIGURE 14.13** ROC curves obtained considering all the 39 patients. In Fig. 14.10A considering the total system resistance during the resting phase; in Fig. 14.10B considering total system resistance when the cuff is inflated.

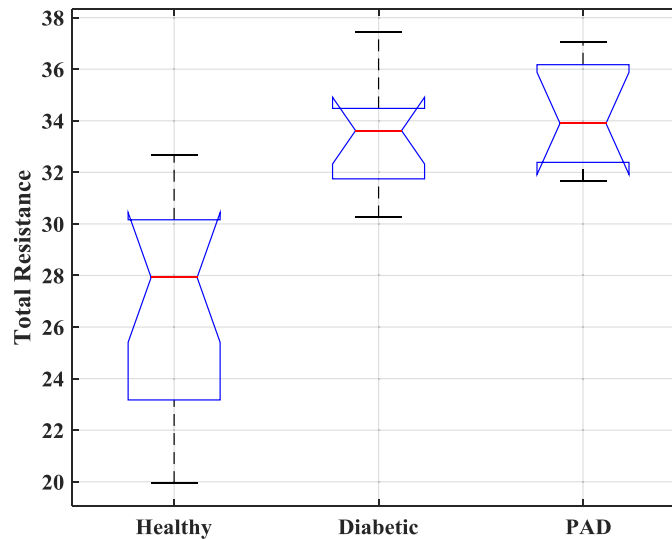
effect is not amplified to the fourth power, and there is a significant variation in the compliances values due to aging [41,44,47,54]. Finally, one cannot evaluate the total capacitance as a simple sum of all the capacitances present, and our clinical data did not contain information about the location of the main calcifications.

p0315 Fig. 14.13 shows the ROC curves for total system resistance R_T as our benchmark parameter. The curves were generated using the data from all 39 subjects (19 healthy subjects, 10 diabetic peripheral artery disease [PAD] patients, and 10 nondiabetic PAD patients). Two ROC curves are shown, one (Fig. 14.13A) for the total resistance during the resting phase ($t = 0$, A) and another one (Fig. 14.13B) for the total resistance when the cuff is inflated ($t = t_{\text{cuff-inflated}}$, B).

p0320 It can be observed that higher sensitivities, specificities and accuracies are obtained when the total resistances are considered during the cuff inflation (see Fig. 14.13B). This is due to the fact that PAD patients' arteries and veins already have smaller internal diameters than in healthy patients and are completely occluded more easily and in less time. Considering the best results obtained when the cuff is inflated, we found a diagnostic sensitivity, specificity, and accuracy of 95%, with an area under the curve $\text{AUC} = 0.97$. These values are considerably higher than the one shown in Fig. 14.8, where a simple heuristic approach was taken that did not include a model of blood flow.

p0325 Among the PAD patients, the 10 nondiabetic patients had an average ABI of 0.64 ± 0.21 indicating moderate disease, whereas the 10 diabetic patients had an average ABI of 0.95 ± 0.35 , which would be misinterpreted as healthy vasculature. We, therefore, performed a statistical ANOVA analysis followed by a paired Bernoulli test using MATLAB embedded functions (anova1 and multcompare) to compare between the three

376 NEUROPHOTONICS AND BIOMEDICAL SPECTROSCOPY

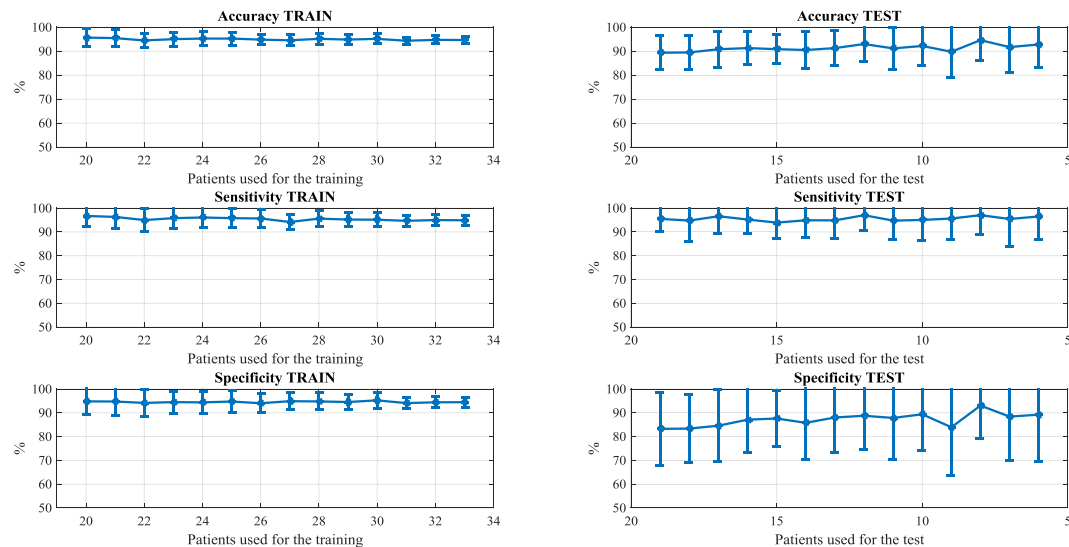


f0075 **FIGURE 14.14** Box plot of the total system resistance during a cuff inflation estimated in healthy, diabetic peripheral artery disease (PAD), and PAD patients.

groups on the basis of their total resistance when the cuff is inflated. The results are shown in Fig. 14.14, where it is possible to see a clear separation between healthy and nondiabetic PAD patients ($P < .8 \times 10^{-5}$) and healthy and diabetic PAD patients ($P < 1.2 \times 10^{-5}$). No statistically significant difference was obtained comparing diabetic and nondiabetic PAD patients.

p0330 A cross-validation analysis, based on a statistical resampling technique used for model assessment, was subsequently carried out to better validate the obtained values for accuracy, sensitivity, and specificity. To determine the optimal cutoff value for the total resistance to differentiate between healthy and PAD patients, a training subset of patients, randomly selected among all the patients, was used and then the remaining patients were used as testing samples to evaluate the model's generalization. This procedure was repeated changing the size of the training subset from 20 to 33 patients. Subsequently, the test subset changed from 19 to 6 patients, and in each case, 500 reshuffling of the random combinations of patients to create the train and test sets were used to increase the objectivity of the assessment, obtaining the mean and standard deviations values showed in Fig. 14.15.

p0335 We observed that, in the training, the mean values were always higher than 90% with standard deviations lower than 5% for all of them, whereas, in the test, accuracy and sensitivity had mean values around 90% with standard deviations lower than 10% and only the specificity had a standard deviation slightly higher (about 16%) and a mean value of about 86%.



f0080 **FIGURE 14.15** Train and test results considering 500 different combinations of patients for each point in the graphs. A number of patients between 20 and 34 was used for the training (on the left) and the remaining patients (from 19 to 6) were used to the test.

s0105 2.5.4 Conclusion

p0340 In this section, we discussed a new model for simulating hemodynamic effects in feet, especially in response to venous cuff occlusions. We demonstrated how this model leads to a better understanding of the hemoglobin variation in the foot observed during vascular optical tomography imaging measurements. Examining data from 19 healthy subjects and 20 PAD patients, we found an inverse correlation between the total system resistance estimated and the healthiness of the patient: the higher the total resistance, the less healthy the patient. This was expected since arteries and veins in healthy subjects should be less obstructed by calcifications as compared to PAD patients; this in turn should result in lower total system resistance to blood flow in healthy subjects.

p0345 The mean values for sensitivity, specificity, and accuracy obtained were in all cases higher than 85%, with a total standard deviation lower than 10% for the accuracy and sensitivity and equal to 15% for the specificity. These values are considerably higher compared to approaches that do not include a model of blood flow. Finally, it is important to note that these results are also higher than typical values reported for other imaging techniques currently under consideration [23,57,58]. Measurements with new patients recording their heart rate, pressure, and timing for the cuff inflation/deflation may help to further increase the fitting precision of the experimental and simulated data and will be the object of future research.

s0110 3. Breast Cancer Imaging

s0115 3.1 Introduction

p0350 Breast cancer affects one in eight women in their lifetime. In the United States, there are approximately 230,000 women with invasive breast cancer and about 40,000 die every year [59]. Neoadjuvant chemotherapy (NAC) is widely applied as standard treatment for patients with newly diagnosed operable invasive breast cancer [60]. The goal of NAC is to shrink the breast tumor prior to surgical intervention. As a result of NAC, an inoperable cancer may become operable or an operable cancer can be converted from mastectomy to breast-conserving therapy. In addition, one of the advantages of NAC is the responsiveness of a patient's breast tumor to systematic therapy can be assessed preoperatively. Pathological response to NAC also associates with breast cancer recurrence and survival. Ideally a pathologic Complete Response (pCR), meaning the complete pathologic disappearance of the tumor before surgery, is achieved. Studies have shown that patients with a pCR have a 90%–95% 5-year survival rate, while 5-year survival rates for patients without pCR are typically below 80% [61]. Depending upon the exact definition, pCR is achieved in only 15%–40% of women. Recent studies have shown that changing therapy in patients that do not show an early response may benefit from a change in treatment regimen [62–67]. Therefore, it would be highly desirable to reliably determine who will and will not respond to NAC early in the treatment [68,69].

p0355 Over the last decade, DOT has emerged as an imaging modality that may be used in breast cancer imaging and is potentially capable of early prediction of treatment outcome [70,71]. DOT uses optical transmission measurements with nonionizing, low-intensity near-infrared light to generate three-dimensional maps of various tissue parameters. Optical property contrast from endogenous chromophores (HbO₂, Hb, water, and lipid) can distinguish malignant from normal tissue [11,12,72,73]. For example, it has been reported that total hemoglobin (HbT) levels, which relate to tumor blood vessel density, are twice as high in malignant tumors as compared to benign breast lesions [74]. Furthermore, studying small animal models of tumors, it was reported that vascular changes precede measurable structure changes [75].

p0360 Given the noninvasive character of this imaging modality and its sensitivity to blood-dependent parameters and tissue vascularity, several groups have started to evaluate DOT or nontomographic diffuse optical spectroscopy (DOS) for monitoring response to NAC. For example, Ueda et al. correlated the pCR rates to baseline tumor oxygen saturation measurements obtained with a handheld spectroscopic measurement system [76]. The handheld probe had only one source and one detector that were scanned across a region of interest to take both frequency-domain and steady-state measurements. No optical tomographic reconstruction of the entire breast was performed. Other groups employed tomographic breast imaging systems [77–81]. This includes the Zhu group at the University of Connecticut, who performed ultrasound-guided DOT NAC monitoring studies [82–86], and Dr. Yodh's team at UPENN, who performed a pilot

study in three patients undergoing NAC. They employed a combined frequency and continuous-wave system that uses two parallel plates to hold one of the breasts in place inside a “breast box.” The box is filled with a solution of Intralipid and India Ink that is used as matching fluid and reference medium [80,81]. Several groups [74,77–79,82,84–89] reported that [HbT] levels seem to significantly decrease in patients that show a pCR, in which the changes could occur as early as a few days within commencement of the NAC. As a result, it was suggested that DOT could be used to predict treatment outcome. A somewhat different observation was made by Soliman et al. and Falou et al. Employing DOS, they found an initial increase followed by a decrease in [Hb] and [HbT] during the first 4 weeks of treatment in patients that achieved a pCR after 6 months of NAC [88,90]. However, it should be noted that Falou et al. did not calculate RCB scores and employed a different criterion to identify pCR patient. Using that criterion they reported on 100% sensitivity and specificity when considering [Hb] increases at 4 weeks after treatment initiation ($P < .002$, analyzing a total of 10 features).

p0365 All these optical imaging studies have included patients on multiple different heterogeneous NAC regimens [76,77–79,83,85–90]. Some studies even included chemoradiation therapy [88,90]. Using different treatment regimens for patients in the same cohort may confound some of the observations. For example, different drugs have differing anti-angiogenic effects and may affect optical signals in disparate ways. Only recently, Schaafsma et al. [36] reported on results found in 22 patients who were all treated with the same NAC protocol. All patients received six cycles of docetaxel, doxorubicin, and cyclophosphamide (TAC) with or without zoledronic acid. Using a nontomographic DOS system they investigated the tumor-bearing breast. They found a statistically significant difference in the decrease in HbO₂ and Hb concentrations after the first cycle of NAC between those that achieved a pCR versus those with a partial response.

p0370 Our group has previously used a dynamic VOTI system to observe the hemodynamics of different tumors to determine if a subject had a benign or malignant tumor or no tumor at all. The contrast mechanism that was used for that diagnostic study was a simple breath hold. The quantified hemodynamic time traces showed variation between the healthy and tumor-bearing breasts of subjects compared to those of healthy subjects, which showed similar traces for both breast. Additionally, we observed a more pronounced change in Hb (Δ [Hb]%) in the tumor at the 15 s post breath hold [11].

p0375 Given these promising results, we hypothesized that we will be able to observe the vascular changes that occur in tumors utilizing VOTI early in treatment. The purpose of the study was to identify optical biomarkers that can be employed to predict pathologic response in breast cancer patients during NAC.

s0120 3.2 Materials and Methods

s0125 3.2.1 Study Subjects and Treatment Regimen

p0380 Our study was compliant with the Health Insurance Portability and Accountability Act (HIPAA) and approved by the Institutional Review Board. Each subject gave written

380 NEUROPHOTONICS AND BIOMEDICAL SPECTROSCOPY

informed consent to the study. Between June 2011 and March 2016, we recruited 40 women (age = 42.2 ± 8.2) over the age of 18 years who were diagnosed with stage II or stage III breast cancer in a study in which patients were enrolled prospectively (therefore, we did not know if they would respond to treatment or not). The diagnosis was determined by X-ray mammography and biopsy. The primary tumor had to be at least 1 cm in diameter. Women with metastases were not eligible.

p0385 All women in the study received the same treatment: weekly 12 cycles of taxane (paclitaxel, docetaxel, or abraxane) followed by four cycles of doxorubicin and cyclophosphamide every 2 weeks with growth factor support. At the end of the treatment, breast cancer surgery was performed and any remaining tumor mass was removed and evaluated by histopathology. For each person, the residual cancer burden (RCB) score G_{RCB} was calculated [91]. A person was considered having a pCR if the $G_{RCB} \leq 0.5$ (RCB class 0). The RCB score was further classified as RCB-I ($0.5 < G_{RCB} \leq 1.36$), RCB-II ($1.36 < G_{RCB} \leq 3.28$), and RCB-III ($G_{RCB} > 3.28$) [91]. Patient identified as belonging to RCB-III were the least responsive to NAC.

p0390 A detailed list with clinical information for all 40 subjects enrolled in this study is provided in Table 14.2. Given are the age, body mass index (BMI), the menopausal status, the type of tumor as determined by pathology, the stage at time of diagnosis, the location of the tumor (left or right breast), Estrogen Receptors (ER) and Progesterone Receptors (PR) readings, Human epidermal growth factor receptor-2 (HER2) status, tumor dimension as determined by palpation at time of diagnosis, and the patient's RCB class at the end of the study, as determined by pathology just before surgery.

s0130 3.2.2 Diffuse Optical Tomography Instrumentation

p0395 The imager used for this study was a continuous-wave dynamic imaging system that provides full 3D tomographic images of both breasts at a rate faster than 1 s. The system employs light at four different wavelengths ($\lambda = 765$ nm, 808 nm, 835 nm, and 905 nm) that is guided to each breast through 32 source fibers. For each breast the transmitted light is collected by 64 optical fibers that guide the light to 64 Si-photodetectors (64 sources and 128 detectors in total). The detection unit utilizes lock-in detection techniques to decrease noise [12,33]. The patient interface consists of two sets of four concentric rings that hold the source and detector fibers. The fibers are placed around the rings in a source–detector–source–detector pattern. The largest ring can be removed to accommodate smaller breast sizes. The ring sets have been placed on camera mounts so that each ring set can move in different angles to provide the most comfortable settings for the patients. During an imaging session, a woman will be seated in front of the system leaning forward to place her breast into the imaging interface (see Fig. 14.16).

p0400 The raw data obtained from the system were preprocessed by applying a discrete cosine transform filter that uses the first 15 coefficients to reduce high-frequency noise. In a second step, the data belonging to source–detector pairs that showed a signal-to-noise ratio of less than 10 dB is removed. The resulting data set was input to a diffusion theory–based PDE-constrained multispectral imaging algorithm [35]. This algorithm

t0015 **Table 14.2** List With Clinical Information for all 40 Subjects Enrolled in This Study

Age	BMI	Menopausal Status	Type	Stage at Diagnosis	Location	ER	PR	HER2	Tumor Size (cm)	RCB Class
47	27.32	Pre	IDC	T2 N1 M0 (Stage IIB)	Right	0	0	pos	3.1	0
66	29.1	Post	IDC	T1c N1 M0 (Stage IIA)	Right	0	0	pos	2.1	0
45	32.07	Pre	IDC	T3 N1 M0 (Stage IIIA)	Left	5	10	neg	12	0
46	31.98	Post	IDC	T2 N1 M0 (Stage IIB)	Left	2	3	pos	5.5	0
54	32.76	Pre	IDC	T2 N1 M0 (Stage IIB)	Left	5	80	pos	3	0
55	34.78	Post	IDC	T2 N1 M0 (Stage IIB)	Left	0	0	pos	2.2	0
29	27.12	Pre	IDC	T2 N1 M0 (Stage IIB)	Left	2	5	pos	2	0
29	32.23	Pre	IDC	T2 N1 M0 (Stage IIB)	Left	0	5	pos	3	0
65	29.87	Post	IDC	T2 N1 M0 (Stage IIB)	Left	0	0	neg	3.5	0
56	38.83	Post	IDC	T2 N1 M0 (Stage IIB)	Right	75	90	pos	1.7	0
62	29.9	Post	IDC	T1 N1 M0 (Stage IIA)	Left	0	0	neg	1.1	0
41	20.07	Post	IDC	T2 N0 M0 (Stage IIA)	Left	0	0	neg	2.6	0
41	23	Pre	IDC	T2 N1 M0 (Stage IIB)	Left	75	0	neg	2.4	0
31	32.4	Pre	IDC	T1c N1 M0 (Stage IIA)	Left	0	0	neg	2	1
30	22.47	Pre	IDC	T1c N1 M0 (Stage IIA)	Right	30	90	pos	3	1
33	23.9	Pre	IDC	T2 N0 M0 (Stage IIA)	Right	0	0	neg	5.6	2
60	26.95	Pre	IDC	T2 N1 M0 (Stage IIB)	Right	100	100	neg	5.5	2
52	25.4	Pre	IDC	T2 N0 M0 (Stage IIA)	Left	15	50	pos	5	2
60	34.8	Post	ILC	T3 N0 M0 (Stage IIB)	Left	100	51	neg	7	2
40	34.55	Pre	IDC	T2 N1 M0 (Stage IIB)	Left	99	10	pos	5	2
59	28.34	Post	ILC	T3 N0 M0 (Stage IIB)	Right	90	15	neg	6	2
61	27.49	Post	IDC	T3 N1 M0 (Stage IIIA)	Left	5	0	neg	10.5	2
55	31.65	Post	IDC	T1 N1 M0 (Stage IIA)	Left	50	50	neg	2	2
46	20.66	Pre	IDC	T2 N1 M0 (Stage IIB)	Left	70	50	pos	3.8	2
62	22.1	Post	IDC	T2 N1 M0 (Stage IIB)	Right	0	0	neg	3.5	2
49	43.98	Pre	IDC	T1c N1 M0 (Stage IIA)	Right	95	90	neg	4.4	2
50	31.31	Post	IDC	T3 N1 M0 (Stage IIIA)	Left	85	50	neg	5.2	2
36	29.4	Pre	IDC	T3 N2 M0 (Stage IIIA)	Left	95	90	neg	2	2
73	25.69	Post	IDC	T2 N1 M0 (Stage IIB)	Left	100	15	neg	3	3

Continued

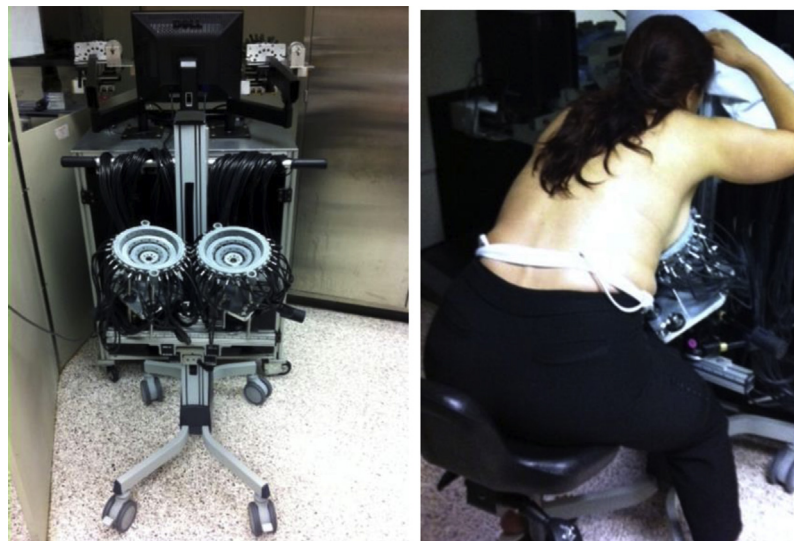
10014-ALFANO-9780323480673

Table 14.2 List With Clinical Information for all 40 Subjects Enrolled in This Study—cont'd

Age	BMI	Menopausal Status	Type	Stage at Diagnosis	Location	ER	PR	HER2	Tumor Size (cm)	RCB Class
50	18.3	Pre	IDC	T2 N1 M0 (Stage IIB)	Right	100	50	pos	3.7	3
61	43.07	Post	ILC	T3 N1 M0 (Stage IIIA)	Left	90	50	neg	9.5	3
47	40.12	Pre	IDC	T3 N3b M0 (Stage IIC)	Left	0	5	neg	7	3
33	29.97	Pre	IDC	T3 N1 M0 (Stage IIIA)	Left	99	99	neg	7	3
40	28.16	Pre	ILC	T2 N1 M0 (Stage IIB)	Right	96	99	neg	10	3
Excluded										
53	31.8	Post	IDC	T2 N1 M0 (Stage IIB)	Left	0	5	neg	7.5	N/A
40	30.18	Post	IDC	T4b N3 M0 (Stage IIC)	Right	<1	10	neg	7	N/A
42	23.32	Pre	IDC	T2 N1 M0 (Stage IIB)	Right	99	80	neg	3.2	0
43	26.81	Post	IDC	T3 N1 M0 (Stage IIIA)	Right	0	0	neg	2.6	0
52	26.81	Pre	IDC	T2 N1 M0 (Stage IIB)	Right	90	90	neg	8	2
66	31.28	Post	IDC	T2 N1 M0 (Stage IIB)	Left	100	95	neg	3.5	2

Given are the age, body mass index (BMI), the menopausal status, the type of tumor as determined by pathology, the stage at time of diagnosis, the location of the tumor (left or right breast), ER and PR readings, HER2 status, tumor size as determined by palpation at time of diagnosis, and Residual Cancer Burden (RCB) class at the end of the study, as determined by pathology just before surgery. Note that IDC stands for ~~Invasive Ductal Carcinoma~~, while ILC stands for ~~Invasive Lobular Carcinoma~~.

10014-ALFANO-9780323480673



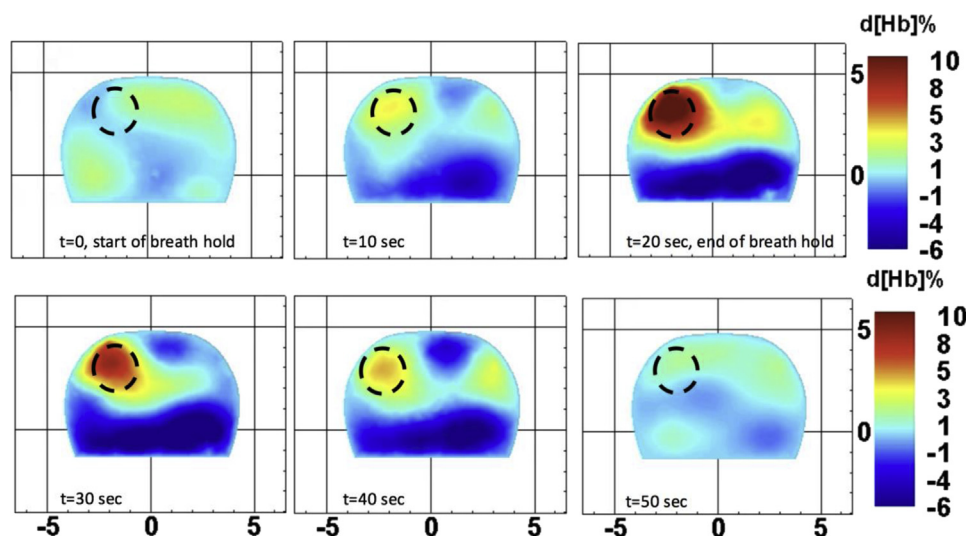
f0085 **FIGURE 14.16** Photos of the imaging system showing the two sets of concentric rings used as patient interface (left) and a patient seated in front of the system leaning forward to place her breasts into the two-ring interface (right).

produced 3-dimensional volumetric images of various tissue parameters of both breasts. In this study we focused on the percent change of HbO₂ concentration (%Δ[HbO₂]) and percent change of Hb concentration (%Δ[Hb]) with respect to values observed at baseline. The baseline values were obtained as the average signal level over a period of 30 s prior to the patient's breath hold.

p0405 The mesh needed for the reconstructions were generated specifically for each individual subject. To this end, the settings for the measurement rings in the imaging interface were recorded prior to the start of the imaging session and subsequently used to generate the patient-specific meshes. The meshes extend 2 cm past the largest ring to account for the effects that the chest wall might have on the reconstruction. Each mesh contained approximately 50,000 to 70,000 elements.

s0135 3.2.3 *Imaging Procedure*

p0410 Dynamic VOTI measurements were performed on all patients just before treatment started and 2 weeks later. After a patient's breasts were placed in the imaging probe, we asked her to remain as still as possible during the image acquisition. Imaging began with a baseline measurement of about 2 min. Next, we imaged the patient while she was holding her breath. We asked patients to hold their breath for up to 30 s. All patients were able to hold their breath for at least 15 s, and all data were included in our analysis. Imaging continued for another 90 s after the patient concluded her breath hold and started breathing again. Each patient performed two or three breath-hold cycles. The total time for the entire imaging procedure was 5–10 min.

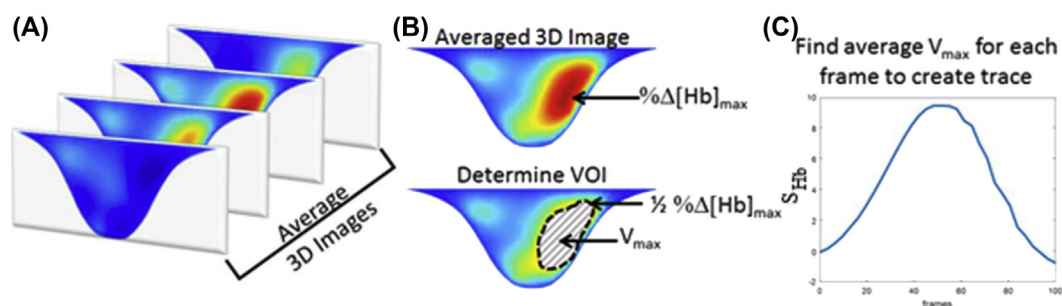


f0090 **FIGURE 14.17** A selection of six images obtained over the course of a 20-s breath hold. Shown are cross-sections through a breast with a tumor (*black circle*) that display the changes in Hb concentrations ($d[\text{Hb}]%$) in percent as compared to baseline during this time. As a patient holds her breath, the blood concentration inside the tumor increases by up to 10% (see image on upper right, $t = 20$ s). Once the patients starts breathing again, the blood concentrations returns back to normal (compare figures for $t = 0$ and $t = 50$ s).

p0415 After the data acquisition was completed, data from one of the breath holds were selected for 3D image reconstruction by one of the researchers (JG, MA) for analysis. The second breath hold was usually chosen, unless substantial patient motion or coughing was observed, in which case the third breath hold was used. Approximately two to three images per second were reconstructed (depending on the number of sources used in imaging the frame rate was 1.74 frame/s [32 sources] to 3.09 frames/s [32 sources]). Averaged data from 30 s before the breath hold was used as a baseline against which changes in Hb and HbO_2 ($S_{\text{Hb}}(t) := \% \Delta [\text{Hb}](t)$ and $S_{\text{HbO}_2}(t) := \% \Delta [\text{HbO}_2](t)$) were calculated. Fig. 14.17 shows a series of images taken over the course of a breath hold. One can clearly see the increase of $S_{\text{Hb}}(t)$ up to the end of the breath hold at 20 s. After that the enhancement decreases.

s0140 3.2.4 Dynamic Data Processing and Feature Extraction

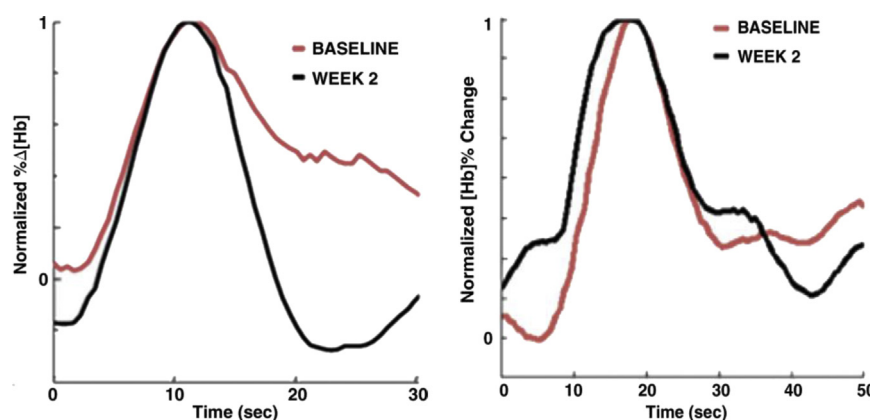
p0420 Based on reconstructed 3D imaging of the two parameters ($\% \Delta [\text{Hb}]$ and $\% \Delta [\text{HbO}_2]$) for both breasts, we assessed the response to NAC. Since time-dependent dynamic data were obtained during a breath hold, we first focused on time-varying features inside the tumor. To identify the area that contains the tumor in the tumor-bearing breast, we average each voxel of the full 3D tomographic data set over the period of the breath hold and half the recovery time. This results in a single frame of 3D data (Fig. 14.18). Within this single frame we determine the location $\vec{x}_{\text{max}} = (x_{\text{max}}, y_{\text{max}}, z_{\text{max}})$ of the maximum percentage change in Hb ($\% \Delta [\text{Hb}]_{\text{max}}$), and the value of half this change is defined as



f0095 **FIGURE 14.18** An overview of how time traces are acquired from 3D imaging. First the frames of the 3D images are averaged (A). Then the maximum percent change in Hb ($\% \Delta [\text{Hb}]_{\text{max}}$) of the averaged 3D image is found (B, top). Next, a VOI (V_{max}) is determined that includes all voxels surrounding $\% \Delta [\text{Hb}]_{\text{max}}$ with a value of at least $\frac{1}{2} \cdot \% \Delta [\text{Hb}]_{\text{max}}$ (B, bottom). Finally, the average of the voxels in the V_{max} for each frame is found and plotted to determine the percent change in Hb signal (S_{Hb}) (C).

$\text{HM} = \% \Delta [\text{Hb}]_{\text{max}}/2$. All voxels within the vicinity of \vec{x}_{max} for which $\% \Delta [\text{Hb}] \geq \text{HM}$ are defined as part of the “volume of interest” (VOI) that contains the region with the tumor. Then for each time point t of the original breath-hold data, the $\% \Delta [\text{Hb}]$ values of each voxel within the VOI is averaged to get a single data point $S_{\text{Hb}}(t) = \% \Delta [\text{Hb}]_{\text{avg}}(t)$. This value will change from time point to time point and a time-dependent curve $S_{\text{Hb}}(t)$ can be plotted (Figure 14.18C). The same process was used to determine $S_{\text{HbO}_2}(t) = \% \Delta [\text{HbO}_2]_{\text{avg}}(t)$.

p0425 Two examples of these curves are shown in Figure 14.19. The graphs show time-dependent signal traces in response to a 30 s breath hold for the tumor region



f0100 **FIGURE 14.19** The two graphs show time-dependent signal traces in response to a 30 s breath hold for the tumor region obtained from dynamic VOTI just before the start of neoadjuvant chemotherapy (NAC) (baseline) and 2 weeks after treatment initiation. (Left) Results from a 46-year-old postmenopausal woman with a poorly differentiated invasive ductal carcinoma with a pathologic Complete Response (pCR) to neoadjuvant chemotherapy (NAC) and was assigned to RCB class 0 (RCB-0). (Right) Results from a 61-year-old postmenopausal woman with a moderately differentiated invasive lobular carcinoma that shows a patient with no response (RCB-III) to NAC.

386 NEUROPHOTONICS AND BIOMEDICAL SPECTROSCOPY

obtained from dynamic VOTI just before the start of NAC (baseline) and 2 weeks after treatment initiation. On the left, results from a 46-year-old postmenopausal woman with a poorly differentiated invasive ductal carcinoma with a pCR, ~~RCB-0~~ to NAC. Her baseline tumor had an initial maximum diameter of 2.9 cm as determined by mammography (a clinical palpation examination found the diameter to be 5.5 cm). Clearly visible is the difference in the curves after the end of the breath hold, where the black and red curves diverge. After 2 weeks of treatment (*black curve*) the %Δ [Hb] returned to pre-breath-hold values much faster than at baseline. This is not the case in the patient who did not respond to therapy, shown on the right. Here results from a 61-year-old postmenopausal woman with a moderately differentiated invasive lobular carcinoma are shown. Employing MRI, it was determined that she had a large tumor of 9.5 cm in diameter, at the start of the therapy. She did not respond well to NAC and was classified as RCB-III at the time of surgery.

p0430 To capture the features of these time-dependent response curves, $S_{\text{Hb}}(t)$ and $S_{\text{HbO}_2}(t)$ in a more quantitative way, we used the following nine parameters, many of which have been used in other dynamic imaging modalities and studies before.

p0435 **Initial enhancement (IE)** is a parameter often employed in functional magnetic resonance imaging (MRI). It is a measure of how an MRI contrast agent increases in signal intensity after injections [92]. We adapted this parameter for dynamic VOTI by defining it as the ratio of the difference between the peak signal strength, S_{peak} , and the initial minimal signal before the peak, S_{initial} , divided the peak signal strength:

$$IE = \frac{S_{\text{peak}} - S_{\text{initial}}}{S_{\text{peak}}} \quad (14.8)$$

p0440 The **post-initial enhancement (PIE)** is another parameter used in contrast-enhance MRI. It is employed to determine how fast a contrast agent leaves a region of interest in DCE-MRI imaging. For dynamic VOTI we define the PIE as

$$PIE = \frac{S_{\text{postBH } 15 \text{ s}} - S_{\text{peak}}}{S_{\text{peak}}} \quad (14.9)$$

p0445 In this equation $S_{\text{postBH } 15 \text{ s}}$ is the [Hb] value 15 s post breath-hold mark. In previous studies we found that this value leads to biggest differences between non-tumor-bearing and tumor-bearing breast [11]. The post-15 value was determined by using the value in the trace 15 s after the peak and normalizing it by the value of the peak.

p0450 The **rise slope, m_{rise}** , was found by using the formula for slope between two points, where the first point was the minimum value before the peak and the second point was the peak point. The **fall slope, m_{fall}** , was similarly found using the peak as the first point and the post-15 s point as the second.

p0455 The **rise rate, q_{rise}** , was determined by fitting the rising portion of the curve to an exponential and taking the rate coefficient by looking at the section between the minimum values before the peak to the peak value. Similarly, the **washout rate, q_{fall}** , was determined by fitting the recovery portion of the breath hold trace to an exponential and taking the rate coefficient. The recovery portion was defined from the maximum point of

the trace to the following minimum position. These portions of the curve were fitted to the following equations:

$$S_X = A_{rise} * e^{q_{rise}*t} \quad (14.10)$$

$$S_X = A_{fall} * e^{-q_{fall}*t}$$

where A_{rise} and A_{fall} were amplitude coefficients, t was the time that has passed in seconds, and S_X is either S_{Hb} or S_{HbO_2} . The parameters q_{rise} and q_{fall} were then used in the current analysis.

p0460 The **normalized maximum peak value (NMPV)** was calculated using the **peak value of the tumor trace**, S_{peak} , normalized by the peak value of the healthy breath hold trace. Furthermore, we calculated the **correlation coefficient (CC)** between the time traces observed in the healthy and tumor-bearing breasts between the corresponding VOI.

s0145 3.2.5 Statistics

p0465 For the statistical analysis of the data we employed the IBM SPSS statistics software package. Given the larger number of features considered (nine parameters that describe $S_{Hb}(t)$ and $S_{HbO_2}(t)$), we first performed a Pearson correlation to determine if there were linear dependencies on any pair of parameters (see Table 14.3). We found particularly strong correlations ($|P_{corr}| > .75$) between all Hb and HbO₂ pairs, meaning that the nine features extracted from the $S_{Hb}(t)$ traces and the related nine features extracted from $S_{HbO_2}(t)$ traces show very strong correlations. Other strong correlations ($|P_{corr}| > .5$, with significance at the 0.01 level) were found between m_{rise} and S_{peak} , q_{fall} and PIE , m_{fall} and m_{rise} and m_{fall} and PIE , and q_{rise} and $NMPV$. Weaker correlations ($0.5 > |P_{corr}| > .35$, with significance at the 0.05 level) were determined for m_{rise} and IE , m_{fall} and q_{fall} , q_{fall} and IE , PIE and S_{peak} .

p0470 Considering feature pairs that are significantly correlated ($P_{corr} > 0.5$), leaves only five features (out of the total 18) that can be considered independent. Applying a Bonferroni correction for multiple comparison results in a 95% confidence interval for $P < .01$ ($=0.05/5$); 90% confidence intervals are reached for $P < .02$ ($=0.1/5$).

p0475 Mean and standard deviation were determined for each of the nine time-trace parameters. One-way ANOVAs were performed for comparison of more than two groups. Otherwise, two-way unpaired student t-tests between designated groups were performed. ROC curves were developed for specified features. The sensitivity, specificity, area under the curve (AUC), accuracy, positive predictive value (PPV), and negative predictive value (NPV) were determined from the Youden index of the ROC curve. The sensitivity in this paper denotes the percentage of the more responsive group that was diagnosed correctly. Conversely, the specificity denotes the percentage of subjects in the least responsive group that were categorized correctly. The positive predictive value (PPV) is the percent of subjects that were classified as the responsive group that were truly responsive subjects. The NPV is the percent of the subjects that were classified in the least responsive group that truly were in the least responsive group.

t0020 **Table 14.3** Pearson Correlation Coefficients for Nine Parameters That Describe $S_{Hb}(t)$ and $S_{HbO_2}(t)$. Note the Very Strong Correlation Between Hb and HbO₂ Pairs.

Pearson Correlation	$m_{rise}(Hb)$	$m_{rise}(HbO_2)$	$m_{fall}(Hb)$	$m_{fall}(HbO_2)$	$q_{rise}(Hb)$	$q_{rise}(HbO_2)$	$q_{fall}(Hb)$	$q_{fall}(HbO_2)$	$IE(Hb)$	$IE(HbO_2)$	$PIE(Hb)$	$PIE(HbO_2)$	$S_{peak}(Hb)$	$S_{peak}(HbO_2)$	$NMPV(Hb)$	$NMPV(HbO_2)$	$CC(Hb)$	$CC(HbO_2)$
$m_{rise}(Hb)$	1	0.944 ^b	-0.482 ^b	-0.478 ^b	0.339 ^a	0.23	0.064	-0.046	0.365 ^a	0.328	0.162	0.201	0.674 ^b	0.662 ^b	0.228	0.225	-0.22	-0.326
$m_{rise}(HbO_2)$	0.944 ^b	1	-0.525 ^b	-0.541 ^b	0.226	0.199	0.072	-0.1	0.388 ^a	0.357 ^a	0.137	0.218	0.720 ^b	0.772 ^b	0.04	0.037	-0.234	-0.314
$m_{fall}(Hb)$	-0.482 ^b	-0.525 ^b	1	0.829 ^b	-0.137	-0.154	-0.429 ^a	-0.208	-0.294	-0.269	0.500 ^b	0.520 ^b	-0.285	-0.364 ^a	0.047	0.046	0.132	0.19
$m_{fall}(HbO_2)$	-0.478 ^b	-0.541 ^b	0.829 ^b	1	0.01	0.016	-0.365 ^a	-0.147	-0.319	-0.205	0.346 ^a	0.448 ^b	-0.278	-0.541 ^b	0.083	0.082	0.04	0.077
$q_{rise}(Hb)$	0.339 ^a	0.226	-0.137	0.01	1	0.854 ^b	-0.03	-0.038	0.323	0.324	-0.032	0.024	-0.061	-0.101	0.546 ^b	0.547 ^b	-0.082	-0.053
$q_{rise}(HbO_2)$	0.23	0.199	-0.154	0.016	0.854 ^b	1	-0.058	-0.049	0.318	0.335	0.044	0.04	-0.103	-0.135	0.355 ^a	0.357 ^a	-0.189	-0.148
$q_{fall}(Hb)$	0.064	0.072	-0.429 ^a	-0.365 ^a	-0.03	-0.058	1	0.750 ^b	0.439 ^b	0.382 ^a	-0.707 ^b	-0.632 ^b	-0.223	-0.132	-0.152	-0.144	-0.092	-0.064
$q_{fall}(HbO_2)$	-0.046	-0.1	-0.208	-0.147	-0.038	-0.049	0.750 ^b	1	0.408 ^a	0.486 ^b	-0.375 ^a	-0.689 ^b	-0.343 ^a	-0.338	-0.144	-0.14	0.083	0.077
$IE(Hb)$	0.365 ^a	0.388 ^a	-0.294	-0.319	0.323	0.318	0.439 ^b	0.408 ^a	1	0.934 ^b	-0.109	-0.092	-0.095	0.028	-0.026	-0.024	-0.067	-0.009
$IE(HbO_2)$	0.328	0.357 ^a	-0.269	-0.205	0.324	0.335	0.382 ^a	0.486 ^b	0.934 ^b	1	-0.024	-0.117	-0.07	-0.033	-0.043	-0.043	-0.091	-0.047
$PIE(Hb)$	0.162	0.137	0.500 ^b	0.346 ^a	-0.032	0.044	-0.707 ^b	-0.375 ^a	-0.109	-0.024	1	0.753 ^b	0.352 ^a	0.235	0.078	0.065	-0.067	-0.084
$PIE(HbO_2)$	0.201	0.218	0.520 ^b	0.448 ^b	0.024	0.04	-0.632 ^b	-0.689 ^b	-0.092	-0.117	0.753 ^b	1	0.410 ^a	0.31	0.111	0.102	-0.155	-0.13
$S_{peak}(Hb)$	0.674 ^b	0.720 ^b	-0.285	-0.278	-0.061	-0.103	-0.223	-0.343 ^a	-0.095	-0.07	0.352 ^a	0.410 ^a	1	0.893 ^b	-0.035	-0.043	-0.149	-0.272
$S_{peak}(HbO_2)$	0.662 ^b	0.772 ^b	-0.364 ^a	-0.541 ^a	-0.101	-0.135	-0.132	-0.338	0.028	-0.033	0.235	0.31	0.893 ^b	1	-0.086	-0.091	-0.106	-0.193
$NMPV(Hb)$	0.228	0.04	0.047	0.083	0.546 ^b	0.355 ^a	-0.152	-0.144	-0.026	-0.043	0.078	0.111	-0.035	-0.086	1	0.999 ^b	0.038	-0.013
$NMPV(HbO_2)$	0.225	0.037	0.046	0.082	0.547 ^b	0.357 ^a	-0.144	-0.14	-0.024	-0.043	0.065	0.102	-0.043	-0.091	0.999 ^b	1	0.038	-0.012
$CC(Hb)$	-0.22	-0.234	0.132	0.04	-0.082	-0.189	-0.092	0.083	-0.067	-0.091	-0.067	-0.155	-0.149	-0.106	0.038	0.038	1	0.910 ^b
$CC(HbO_2)$	-0.326	-0.314	0.19	0.077	-0.053	-0.148	-0.064	0.077	-0.009	-0.047	-0.084	-0.13	-0.272	-0.193	-0.013	-0.012	0.910 ^b	1

^adenotes that correlation is significant at the 0.05 level (2-tailed).

^bdenotes that correlation is significant at the 0.01 level (2-tailed).

s0150 3.3 Results

s0155 3.3.1 Patient Summary

p0480 Of the 40 patients enrolled in the study, results from six patients were not included in the analysis presented here. One patient completely stopped NAC midway through the therapy and was removed from the study. Two subjects missed their week 2 imaging time point. For another two subjects, instrumentation failure during the imaging session resulted in corrupted data sets that could not be used. Finally, one subject opted to receive radiation therapy in addition to the traditional NAC therapy and therefore was removed from the analysis.

p0485 The average age of the remaining 34 patients was 49 years. There were 19 premenopausal subjects and 15 postmenopausal subjects. Four subjects were diagnosed with an invasive lobular carcinoma, and 29 patients had an invasive ductal carcinoma. One subject had mixed invasive lobular and ductal carcinoma. Using the largest measurable dimension as size metric, the average initial tumor size was 4.6 ± 2.8 cm, based on baseline clinical examinations. After NAC, 13 subjects were classified as RCB-0 (i.e., pCR). Two patients were classified as RCB-I, 13 subjects as RCB-II, and six subjects as RCB-III. Table 14.2 provides a full summary of the clinical and pathologic features.

s0160 3.3.2 Statistical Analysis of Hemoglobin Traces Observed at Week 2

p0490 Table 14.4 shows the data for all four cohorts (RCB-0, I, II, III) for all nine features (IE , PIE , m_{rise} , m_{fall} , q_{rise} , q_{fall} , S_{peak} , $NMPV$, and CC) for the $S_{Hb}(t)$ and $S_{HbO_2}(t)$ response curves 2 weeks after treatment initiation. The m_{rise} , S_{peak} , $NMPV$, and CC do not show statistically significant difference between the response groups. Only features related to $S_{Hb}(t)$ show some statistically significant differences ($P < .01$ for 95% confidence interval, and $P < .02$ for 90% confidence intervals) between groups. These include IE ($P < .013$ for RCB 0,I,II vs. RCB III), PIE ($P < .004$ for RCB 0 vs. RCB I,II,II and $P < .007$ for RCB 0,I vs. RCB II,II), m_{fall} ($P < .006$ for RCB 0 vs. RCB I,II,II and $P < .002$ for RCB 0,I vs. RCB II,II), and q_{fall} ($P < .003$ for RCB 0 vs. RCB I,II,II and $P < .015$ for RCB 0,I vs. RCB II,II).

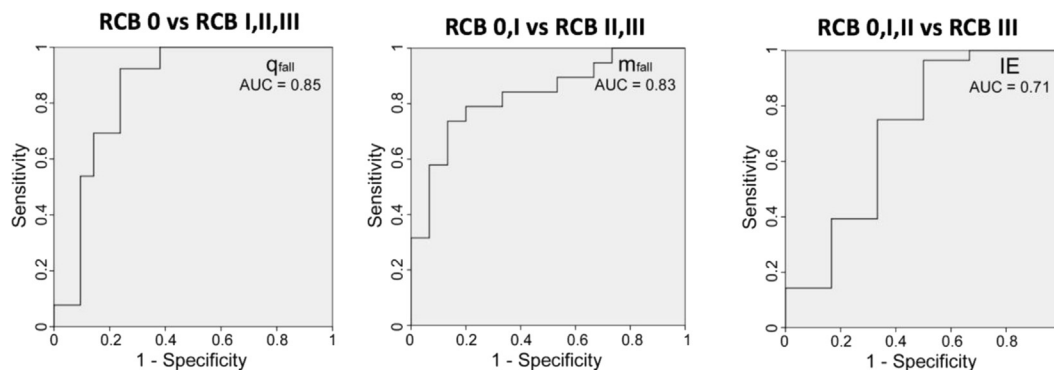
p0495 Since the difference in q_{fall} for S_{Hb} traces between patients with a pCR (RCB-0) and non-pCR (RCB-I,-II,-III) produced the strongest statistically significant distinction ($P < .003$), we created an ROC curve for this variable (Fig. 14.20). The sensitivity, specificity, and accuracy are 92.3% (12/13 subjects), 76% (16/21 subjects), and 82.4% (28/34 subjects), respectively (cutoff point $q_{fall} = 0.09$). The AUC was 0.85, and the PPV was calculated to be 70.6% (12/17 subjects) with the NPV 94.1% (16/21 subjects). Similar ROC curves and analyses for m_{fall} , PIE , IE , and q_{rise} for S_{Hb} resulted in values shown in Fig. 14.20 and Table 14.5.

p0500 To specifically find RCB-III patients, the best features seem to be IE ($P < .013$) and q_{rise} ($P < .027$) for the S_{Hb} traces. The AUC for IE and q_{rise} is 0.71 and 0.83, respectively. The parameter IE yields high sensitivity of 96.4% (27/28) and high PPV of 90.0% (27/30), while the use of q_{rise} yields high specificity of 100% (6/6) and high PPV of 100% (15/15).

Table 14.4 Summary of the Mean Values and Standard Deviations for All Four RCB Classes for Features Derived From Time Traces of the Hemodynamic Responses, $S_{Hb}(t)$ and $S_{HbO_2}(t)$, Obtained 2 Weeks After the Initial Treatment With Taxane

Features	Time Traces	RCB 0	RCB 1	RCB II	RCB III	ANOVA 1 (4 Groups)	ANOVA 2 (3 Groups 0 and I)	ANOVA 3 (3 Groups I and II)	pCR vs. Non-pCR		
									(RCB 0 vs. RCB I, II, and III)	RCB 0 and I vs. RCB II and III	RCB 0, I, and II vs. RCB III
<i>IE</i>	S_{Hb}	1.02 ± 0.28	0.92 ± 0.04	0.96 ± 0.15	0.71 ± 0.34	0.09	0.04	0.04	0.13	0.15	0.013
	S_{HbO_2}	1.03 ± 0.29	0.90 ± 0.03	0.96 ± 0.18	0.73 ± 0.35	0.14	0.08	0.07	0.13	0.17	0.03
<i>PIE</i>	S_{Hb}	-0.89 ± 0.52	-0.51 ± 0.18	-0.40 ± 0.42	-0.30 ± 0.56	0.04	0.02	0.01	0.004	0.007	0.15
	S_{HbO_2}	-0.77 ± 0.38	-0.47 ± 0.21	-0.49 ± 0.46	-0.44 ± 0.48	0.30	0.24	0.15	0.052	0.09	0.37
m_{rise}	S_{Hb}	0.80 ± 0.83	0.47 ± 0.21	0.70 ± 0.49	0.38 ± 0.46	0.58	0.46	0.41	0.34	0.47	0.22
	S_{HbO_2}	0.44 ± 0.47	0.24 ± 0.06	0.32 ± 0.20	0.17 ± 0.15	0.39	0.30	0.23	0.14	0.21	0.17
m_{fall}	S_{Hb}	-0.46 ± 0.32	-0.41 ± 0.31	-0.19 ± 0.20	-0.01 ± 0.34	0.015	0.005	0.008	0.006	0.002	0.028
	S_{HbO_2}	-0.24 ± 0.25	-0.19 ± 0.13	-0.11 ± 0.12	-0.03 ± 0.14	0.11	0.05	0.054	0.03	0.02	0.09
q_{rise}	S_{Hb}	0.11 ± 0.06	0.07 ± 0.004	0.17 ± 0.10	0.05 ± 0.04	0.03	0.01	0.04	0.70	0.43	0.027
	S_{HbO_2}	0.12 ± 0.06	0.07 ± 0.01	0.17 ± 0.10	0.08 ± 0.06	0.10	0.06	0.17	0.61	0.32	0.13
q_{fall}	S_{Hb}	0.18 ± 0.09	0.07 ± 0.02	0.09 ± 0.10	0.07 ± 0.07	0.03	0.05	0.01	0.003	0.015	0.16
	S_{HbO_2}	0.17 ± 0.14	0.07 ± 0.04	0.11 ± 0.10	0.11 ± 0.07	0.38	0.44	0.23	0.09	0.20	0.59
S_{peak}	S_{Hb}	9.24 ± 7.54	11.0 ± 5.21	8.61 ± 5.31	9.26 ± 8.31	0.97	0.94	0.99	0.93	0.77	0.95
	S_{HbO_2}	5.34 ± 5.29	5.62 ± 1.66	4.34 ± 3.29	3.98 ± 3.82	0.88	0.72	0.78	0.50	0.42	0.63
<i>NMPV</i>	S_{Hb}	1.83 ± 1.62	1.16 ± 0.85	1.55 ± 1.24	2.93 ± 4.27	0.61	0.43	0.41	0.44	0.37	0.73
	S_{HbO_2}	1.85 ± 1.51	0.81 ± 0.26	1.32 ± 0.95	2.57 ± 3.39	0.48	0.39	0.31	0.75	0.97	0.20
<i>CC</i>	S_{Hb}	0.46 ± 0.38	0.57 ± 0.17	0.36 ± 0.34	0.43 ± 0.36	0.34	0.52	0.96	0.77	0.28	0.93
	S_{HbO_2}	0.53 ± 0.37	0.69 ± 0.26	0.41 ± 0.34	0.39 ± 0.37	0.47	0.42	0.69	0.45	0.19	0.50

CC, correlation coefficient; *IE*, initial enhancement; m_{fall} , fall slope; m_{rise} , rise slope; *NMPV*, normalized maximum peak value; *PIE*, post-initial enhancement; q_{rise} , rise rate; q_{fall} , washout rate; S_{peak} , peak signal. Furthermore, *P*-values are shown for various statistical analyses. Value of $P < .01$ indicated statistical significance (95% confidence interval - 90% confidence intervals are reached for $P < .02$).



f0105 **FIGURE 14.20** Shown are three ROC curves related to the three features in Table 14.4 that produces low p-values. The left-most figures shows the ROC curve for features q_{fall} that allows to best distinguish between classes RCB 0 and RCB I,II,III. The figure in the middle shows an ROC curve for the feature m_{fall} that best distinguishes between classes RCB 0 and I and RCB II and III. Finally, the figure on the right shows the ROC curve for the features IE , which best distinguishes class RCB 0, I, and II from RCB III.

t0030 **Table 14.5** Summary of Binary Classification Test for the Features That Show the Statistically Most Significant Differences Between Subject Groups Based on an Analysis of the Data Obtained at Week 2 From the Percent Change in Deoxyhemoglobin Signal, S_{Hb} (t) (see Table 14.4, Last Three Columns)

RCB 0 vs. I, II and III	Sensitivity	Specificity	Accuracy	AUC	PPV	NPV
q_{fall}	92.3% (12/13)	76.2% (16/21)	82.4% (28/34)	0.85	70.6% (12/17)	94.1% (16/17)
PIE	61.5% (8/13)	90.5% (19/21)	79.4% (27/34)	0.79	80.0% (8/10)	79.2% (19/24)
RCB 0 and I vs. II and III	Sensitivity	Specificity	Accuracy	AUC	PPV	NPV
m_{fall}	86.7% (11/15)	73.7% (16/19)	79.4% (27/34)	0.83	78.6% (11/14)	80.0% (16/20)
PIE	68.4% (10/15)	80% (15/19)	73.53% (25/34)	0.77	71.5% (10/14)	75.0% (15/20)
RCB 0, I and, II vs. III	Sensitivity	Specificity	Accuracy	AUC	PPV	NPV
IE	96.4% (27/28)	50.0% (3/6)	88.2% (30/34)	0.71	90.0% (27/30)	75.0% (3/4)
Q_{rise}	53.6% (15/28)	100% (6/6)	61.8% (21/34)	0.83	100.0% (15/15)	31.6% (6/19)

AUC, area under the curve; IE , initial enhancement; M_{fall} , fall slope; NPV, negative predictive value; PIE , post-initial enhancement; PPV, positive predictive value; Q_{fall} , fall rate; Q_{rise} , rise rate; RCB, residual cancer burden.

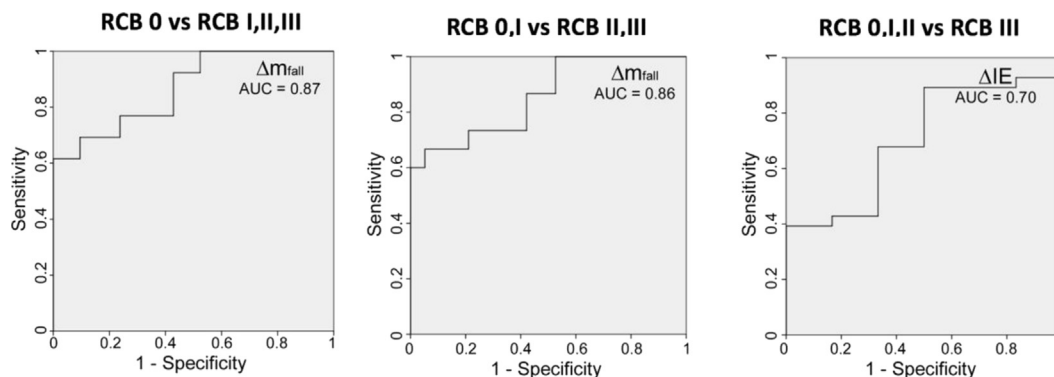
s0165 3.3.3 Statistical Analysis of Differences Between Baseline and Week 2 Imaging

p0505 In addition to evaluating the hemoglobin traces observed at week 2, we also analyzed differences between data obtained at baseline (week 0) and week 2 (Table 14.6). In this table, the most notable entries are the low P -values for Δm_{fall} determined from S_{Hb} traces and S_{HbO_2} traces. For the clinically meaningful comparison of RCB-0 versus RCB-I, -II, and -III, subjects with a pCR exhibited an increase in Δm_{fall} compared to non-pCR subject (S_{Hb} : $P < .0004$). A ROC curve analysis shows that for Δm_{fall} for S_{Hb} we find that the sensitivity, specificity, and accuracy is 61.5% (8/13 subjects), 100% (21/21 subjects), and 85.3% (29/34 subjects) with an AUC of 0.87 (Fig. 14.21 and Table 14.7).

t0035 **Table 14.6** Summary of the Differences in Features Derived From Time Traces of the Hemodynamic Responses, $S_{Hb}(t)$ and $S_{HbO_2}(t)$, Between Baseline and Two Weeks After the Initial Treatment With Taxane (Week 2—Baseline)

Features	Time Traces	RCB 0	RCB I	RCB II	RCB III	ANOVA 1 (4 Groups)	ANOVA 2 (3 Groups 0 and I)	ANOVA 3 (3 Groups I and II)	pCR vs. Non-pCR (RCB 0 vs. RCB I, II, and III)	RCB 0&I vs. RCB II and III	RCB 0, I, and II vs. RCB III
ΔIE	S_{Hb}	0.03 ± 0.39	-0.39 ± 0.27	-0.04 ± 0.30	-0.29 ± 0.31	0.16	0.28	0.19	0.17	0.47	0.11
	S_{HbO_2}	0.16 ± 0.38	-0.35 ± 0.49	0.03 ± 0.41	-0.40 ± 0.37	0.03	0.05	0.02	0.055	0.18	0.01
ΔPIE	S_{Hb}	0.29 ± 0.66	0.15 ± 0.45	-0.25 ± 0.70	0.02 ± 0.53	0.23	0.12	0.15	0.068	0.056	0.97
	S_{HbO_2}	0.17 ± 1.08	0.08 ± 0.77	-0.25 ± 0.54	0.02 ± 0.64	0.63	0.42	0.48	0.28	0.26	0.87
ΔM_{rise}	S_{Hb}	0.47 ± 0.65	-0.06 ± 0.01	-0.13 ± 1.08	-0.07 ± 0.26	0.27	0.20	0.14	0.045	0.071	0.55
	S_{HbO_2}	0.26 ± 0.36	0.003 ± 0.001	-0.03 ± 0.51	-0.07 ± 0.14	0.22	0.15	0.11	0.03	0.052	0.34
ΔM_{fall}	S_{Hb}	0.33 ± 0.33	0.03 ± 0.27	-0.38 ± 0.56	-0.13 ± 0.30	0.003	0.001	0.002	0.0004	0.0004	0.64
	S_{HbO_2}	0.16 ± 0.21	-0.08 ± 0.31	-0.12 ± 0.27	-0.06 ± 0.13	0.03	0.03	0.01	0.0025	0.01	0.50
ΔQ_{rise}	S_{Hb}	-0.04 ± 0.14	-0.1 ± 0.21	-0.03 ± 0.19	-0.12 ± 0.22	0.64	0.55	0.60	0.69	0.94	0.31
	S_{HbO_2}	0.002 ± 0.10	-0.13 ± 0.20	0.001 ± 0.18	-0.14 ± 0.12	0.15	0.14	0.13	0.32	0.59	0.05
ΔQ_{fall}	S_{Hb}	0.02 ± 0.14	-0.01 ± 0.05	-0.11 ± 0.19	-0.07 ± 0.12	0.23	0.11	0.16	0.056	0.041	0.70
	S_{HbO_2}	0.01 ± 0.19	-0.01 ± 0.06	-0.14 ± 0.19	-0.06 ± 0.11	0.23	0.11	0.17	0.08	0.055	0.98
ΔS_{peak}	S_{Hb}	-4.44 ± 4.96	-1.32 ± 1.68	2.13 ± 11.6	-3.53 ± 8.58	0.14	0.16	0.56	0.14	0.16	0.56
	S_{HbO_2}	-2.68 ± 3.20	-0.49 ± 2.36	-0.19 ± 6.23	-1.27 ± 4.30	0.20	0.26	0.96	0.20	0.26	0.96
$\Delta NMPV$	S_{Hb}	-0.74 ± 1.83	0.15 ± 0.06	-0.02 ± 1.81	-2.19 ± 4.61	0.37	0.23	0.21	0.88	0.94	0.96
	S_{HbO_2}	-0.63 ± 1.86	0.23 ± 0.23	0.41 ± 1.75	-1.92 ± 3.67	0.22	0.12	0.11	0.70	0.86	0.08
ΔCC	S_{Hb}	0.01 ± 0.41	0.07 ± 0.18	0.22 ± 0.45	-0.04 ± 0.38	0.50	0.32	0.33	0.39	0.41	0.41
	S_{HbO_2}	-0.02 ± 0.45	0.04 ± 0.27	0.07 ± 0.50	0.02 ± 0.33	0.93	0.92	0.83	0.58	0.73	0.98

pCR, pathologic complete response; RCB, residual cancer burden; ΔCC , change in correlation coefficient; ΔIE , change in initial enhancement; ΔM_{fall} , change in fall slope; ΔM_{rise} , change in rise slope; $\Delta NMPV$, change in normalized maximum peak value; ΔPIE , change in post-initial enhancement; ΔQ_{fall} , change in washout rate; ΔQ_{rise} , change in rise rate; ΔS_{peak} , change in peak signal.



f0110 **FIGURE 14.21** Shown are three ROC curves related to the three features in Table 14.7 that produces low p-values. The left-most figures shows the ROC curve for features Δm_{fall} that allows to best distinguish between classes RCB 0 and RCB I, II, and III. The figure in the middle shows also a ROC curve for the feature Δm_{fall} . In this case the feature is used to distinguish between classes RCB 0 and I and RCB II and III. Finally, the figures on the right shows the ROC curve for the features ΔIE , which best distinguishes class RCB 0, I, and II from RCB III.

t0040 **Table 14.7** Summary of Binary Classification Test for the Features That Show the Statistically Most Significant Differences Between Subject Groups Based on Features Derived From Time Traces of the Hemodynamic Responses, $S_{Hb}(t)$, Between Baseline and Two Weeks After the Initial Treatment With Taxane (See Table 14.6, Last three Columns)

RCB 0 vs. I, II, and III	Sensitivity	Specificity	Accuracy	AUC	PPV	NPV
Δm_{rise}	84.6% (11/13)	57.1% (12/21)	67.6% (23/34)	0.71	55.0% (11/20)	85.7% (12/14)
Δm_{fall}	61.5% (8/13)	100% (21/21)	85.3% (29/34)	0.87	100% (8/8)	80.8% (21/26)
RCB 0 and I vs. II and III	Sensitivity	Specificity	Accuracy	AUC	PPV	NPV
Δm_{fall}	66.7% (10/15)	94.7% (18/19)	82.4% (28/34)	0.86	90.9% (10/11)	78.3% (18/23)
Δq_{fall}	73.3% (11/15)	78.9% (15/19)	76.5% (26/34)	0.76	73.3% (11/15)	78.9% (15/19)
RCB 0, I, and II vs. III	Sensitivity	Specificity	Accuracy	AUC	PPV	NPV
ΔIE	73.3% (20/28)	66.7% (4/6)	70.6% (24/34)	0.70	90.9% (20/22)	33.3% (4/12)
Δq_{rise}	50.0% (14/28)	83.3% (5/6)	55.9% (19/34)	0.83	93.3% (14/15)	26.3% (5/19)

RCB, residual cancer burden; ΔIE , change in initial enhancement; Δm_{rise} , change in rise slope; Δm_{fall} , change in fall slope; Δq_{rise} , change in rise rate; Δq_{fall} , change in washout rate.

The PPV was 100% (8/8 subjects), and the NPV was 80.8% (21/26 subjects). The 100% specificity signifies that all the patients with a non-pCR were identified as having a non-pCR response. This is of particular importance, as these are exactly the patients who would benefit from a change in therapy.

s0170 3.4 Discussion

p0510 We describe a relatively large cohort of patients in which as subjects follow the same NAC regimen, a standard taxane-/anthracycline-based therapy. Our optical imaging

394 NEUROPHOTONICS AND BIOMEDICAL SPECTROSCOPY

system performs 3-dimensional dynamic VOTI that provides information about hemodynamic effects on both breasts simultaneously. This allows for a direct comparison of the tumor-bearing breast and the non-tumor-bearing breast of the same patients.

p0515 Our study showed that tumors in patients with pCR (RCB = 0) have higher washout rates, q_{fall} , by week 2 compared to non-pCR (RCB = I, II, III) patients. Using q_{fall} for S_{Hb} as parameter to predict patients with a pCR, we achieved a sensitivity of 92.3% (12/13 subjects) and a specificity of 76% (16/21 subjects). Additionally, Δm_{fall} of the S_{Hb} trace showed significant difference between pCR and non-pCR subjects. This may possibly indicate an increase in blood flow in the tumor. For this analysis, the highest AUC (0.87) and specificity (100% (21/21 subjects)) were obtained.

p0520 Like many other chemotherapeutic drugs, taxanes disrupts the cell cycle to prevent proliferation and causes apoptosis. In addition it has been shown that taxanes disrupts microvessels and decreases microvascular density [93]. However, instead of disrupting blood flow, studies in mice have suggested that the diameter of the tumor vessel and blood flow velocity inside the vessels actually increase when a tumor responds to taxanes. To explain this apparent paradox, it has been argued that solid tumors have a naturally high interstitial fluid pressure due to the compression of blood vessels from surrounding tumor cells, the disorganized tumor vascular network, and the absence of functional lymphatics [94–96]. Chemotherapy leads to a reduction of tumor cell density, which in turn lowers interstitial fluid pressure, and consequently increasing blood vessel diameter and blood flow velocity. These arguments are supported by another study that demonstrated that interstitial fluid pressure decreased after breast cancer patients who received the taxane paclitaxel [97].

p0525 We saw statistically significant increases in m_{fall} for pCR subjects between the baseline and week 2 imaging time point suggesting that there may be increase blood flow in the tumor. Therefore, there is evidence in this study to suggest that the increase apoptosis and decrease interstitial fluid pressure in responding tumors to taxane may cause the increase in m_{fall} by the second week of NAC and could be physiologically relevant parameters.

p0530 Our study had limitations. Some subjects could not hold their breath for the entire desired length of 30 s. Not surprisingly, curve parameters that are not dependent on the breath-hold length such as normalized peak values and washout rates yielded more promising results than parameters that would depend on breath-hold. Furthermore, as a minimum tumor size of 1-cm in diameter was required for study participation, no statement can be made on how well this method works for smaller tumors. Also, other nontaxane-based treatment regimens will need to be tested, and the influence of different types of drugs on outcome predictability is a goal for future studies. Finally, this has been a pilot study to identify most promising imaging parameters. Hence, we used our data to determine threshold for the various dynamic imaging features. This can lead to an overestimation of the results. A follow-up prospective study with a larger cohort that produces an independent data set is needed to confirm our findings.

p0535 In conclusion, we have developed an imaging approach to noninvasively extract information about the hemodynamic effects that occur in and around tumors of breast cancer patients. In this study we demonstrate that certain features of the hemodynamic responses to a simple breath hold can be used to predict treatment outcome in patients undergoing NAC. Using q_{fall} for S_{Hb} as parameter to predict patients with a pCR, we achieved a sensitivity of 92.3% (12/13) and a specificity of 76% (16/21). Additionally, the difference in m_{fall} of S_{Hb} traces between the two imaging points showed significant difference between pCR and non-pCR subjects, where pCR subjects showed an increase. Finally, we determined that q_{rise} of the S_{Hb} trace is the best feature for comparing RCB-0/I/II versus RCB III patients, i.e., the patients at highest risk for breast cancer, in this case, were able to get 100% (6/6 subjects) specificity, which indicates that we can identify all nonresponders. These are subjects that are least likely to respond NAC and hence may be prime candidates for a change of therapy.

Acknowledgments

For their contributions to the breast cancer imaging study we would like to thank Jacqueline E. Gunther and Molly Flexman, both PhD students in Dr. Hielscher's laboratory, as well as the clinical collaborators from the Department of Medicine – Division of Hematology/Oncology at the Columbia University Irving Medical Center, which includes Dr. Emerson Lim, Dr. Jessica A. Campbell, Dr. Hanina Hibshoosh, Dr. Katherine Crew, Dr. Kevin Kalinsky, and Dr. Dawn L. Hershman. For their contributions to the studies related to peripheral artery disease we would like to thank Michael A. Khalil, Christopher Fong, and Jennifer Hoi, all PhD students in Dr. Hielscher's laboratory, as well as the clinical collaborators from the Department of Surgery – Division of Vascular Surgery and Endovascular Intervention at the Columbia University Irving Medical Center, which includes Dr. Danielle Bajakian, Dr. Gautam Shrikhande, and Dr. Rajeev Dayal. This work was supported in part by grants from the National Heart, Lung, and Blood Institute (NHLBI- 1R01-HL115336-01) at the National Institutes of Health (NIH), the Society of Vascular Surgery, and the Wallace H. Coulter Foundation. Furthermore, Alessandro Marone, PhD, was supported in part by a fellowship for translational research from the School of Engineering and Applied Science (SEAS) at Columbia University in the City of New York; and Mirella L. Altoé was supported in part by a scholarship from the Brazilian Department of Higher Education of the Ministry of Education, and the Ministry of Science, Technology and Innovation (Science Without Borders/Latin American Scholarship Program of American Universities (LASPAU)).

References

- [1] Hielscher AH, et al. Near-infrared diffuse optical tomography. *Dis Markers* 2002;18(5–6):313–37.
- [2] Hebden JCA, Arridge SR, Delpy DT. Optical imaging in medicine .I. Experimental techniques. *Phys Med Biol* 1997;42(5):825–40.
- [3] Schmitz CHL, Lasker M, Hielscher JM, Barbour AH, R.L. Instrumentation for fast functional optical tomography. *Rev Sci Instrum* 2002;73(2):429–39.
- [4] Pogue BW, et al. Quantitative hemoglobin tomography with diffuse near-infrared spectroscopy: pilot results in the breast. *Radiology* January 2001;218(1):261–6.

396 NEUROPHOTONICS AND BIOMEDICAL SPECTROSCOPY

- [5] McBride TOP, Brain W, Jiang S, Österberg UL, Paulsen KD. A parallel-detection frequency domain near-infrared tomography system for hemoglobin imaging of the breast in vivo. *Rev Sci Instrum* 2001;72:1817–24.
- [6] Boas D, Gaudette T, Arridge S. Simultaneous imaging and optode calibration with diffuse optical tomography. *Optics Express* February 26, 2001;8(5):263–70.
- [7] Jiang H, Iftimia NV, Xu Y, Eggert JA, Fajardo LL, Klove KL. Near-infrared optical imaging of the breast with model-based reconstruction. *Acad Radiol* February 2002;9(2):186–94.
- [8] Hoshi Y. Hemodynamic signals in fNIRS. In: Masamoto KH, Yamada KH, editors. *New Horizons in Neurovascular Coupling: A Bridge Between Brain Circulation and Neural Plasticity*. Elsevier; 2016. p. 153–79. *Progress in brain research*, no. 225.
- [9] Schmitz CH, et al. Design and implementation of dynamic near-infrared optical tomographic imaging instrumentation for simultaneous dual-breast measurements. *Appl Optics* April 10, 2005; 44(11):2140–53.
- [10] ~~Gunther JE, et al. Dynamic diffuse optical tomography for monitoring neoadjuvant chemotherapy in patients with breast cancer. *Radiology* February 12, 2018:161041.~~
- [11] Flexman ML, et al. Optical biomarkers for breast cancer derived from dynamic diffuse optical tomography. *J Biomed Optics* September 2013;18(9):096012.
- [12] Flexman ML, et al. Digital optical tomography system for dynamic breast imaging. *J Biomed Optics* July 2011;16(7):076014.
- [13] Erickson-Bhatt SJ, et al. Noninvasive surface imaging of breast cancer in humans using a hand-held optical imager. *Biomed Phys Eng Express* December 2015;1(4).
- [14] Lasker JM, Fong CJ, Ginat DT, Dwyer E, Hielscher AH. Dynamic optical imaging of vascular and metabolic reactivity in rheumatoid joints. *J Biomed Optics* September-October;12(5):052001.
- [15] Wu HY, Filer A, Styles I, Dehghani H. Development of a multi-wavelength diffuse optical tomography system for early diagnosis of rheumatoid arthritis: simulation, phantoms and healthy human studies. *Biomed Optics Express* November 1, 2016;7(11):4769–86.
- [16] Khalil MA, et al. Dynamic diffuse optical tomography imaging of peripheral arterial disease. *Biomed Optics Express* September 1, 2012;3(9):2288–98.
- [17] Khalil MA, et al. Detection of peripheral arterial disease within the foot using vascular optical tomographic imaging: a clinical pilot study. *Eur J Vasc Endovasc Surg* January 2015;49(1):83–9.
- [18] Jayachandran M, Rodriguez S, Solis E, Lei J, Godavarty A. Critical review of noninvasive optical technologies for wound imaging. *Adv Wound Care* August 1, 2016;5(8):349–59.
- [19] Godavarty A, Rao PN, Khandavilli Y, Jung YJ. Diabetic wound imaging using a noncontact near-infrared scanner: a pilot study. *J Diabetes Sci Technol* June 17, 2015;9(5):1158–9.
- [20] Hirsch AT, et al. Peripheral arterial disease detection, awareness, and treatment in primary care. *J Am Med Assoc* September 19, 2001;286(11):1317–24.
- [21] Hiatt WR. Medical treatment of peripheral arterial disease and claudication. *N Engl J Med* May 24, 2001;344(21):1608–21.
- [22] Norgren L, Hiatt WR, Dormandy JA, Nehler MR, Harris KA, Fowkes FGR. "Inter-society consensus for the management of peripheral arterial disease (TASC II)," (in English). *Eur J Vasc Endovasc Surg* 2007;33:S5–75.
- [23] Al-Qaisi M, Nott DM, King DH, Kaddoura S, Hamady M. Imaging of peripheral vascular disease. *Rep Med Imag* 2009;2:25–34.
- [24] Sanada H, Higashi Y, Goto C, Chayama K, Yoshizumi M, Sueda T. Vascular function in patients with lower extremity peripheral arterial disease: a comparison of functions in upper and lower extremities. *Atherosclerosis* January 2005;178(1):179–85.

Chapter 14 • Dynamic Vascular Optical Tomographic Imaging 397

- [25] Finn AV, Chandrashekar Y, Narula J. IVUS and OCT: either or survivor. *JACC Cardiovasc Imaging* September 2011;4(9):1047–9.
- [26] Wolf U, et al. Localized irregularities in hemoglobin flow and oxygenation in calf muscle in patients with peripheral vascular disease detected with near-infrared spectrophotometry. *J Vasc Surg* May 2003;37(5):1017–26.
- [27] Casavola C, Paunescu LA, Fantini S, Gratton E. Blood flow and oxygen consumption with near-infrared spectroscopy and venous occlusion: spatial maps and the effect of time and pressure of inflation. *J Biomed Optics* July 2000;5(3):269–76.
- [28] Gibson AP, Hebden JC, Arridge SR. Recent advances in diffuse optical imaging. *Phys Med Biol* February 21, 2005;50(4):R1–43.
- [29] Durduran T, Choe R, Baker WB, Yodh AG. Diffuse optics for tissue monitoring and tomography. *Rep Prog Phys* July 2010;73(7).
- [30] Schmitz CH, et al. Instrumentation and calibration protocol for imaging dynamic features in dense-scattering media by optical tomography. *Appl Optics* December 1, 2000;39(34):6466–86.
- [31] Lasker JM, Masciotti JM, Schoenecker M, Schmitz CH, Hielscher AH. Digital-signal-processor-based dynamic imaging system for optical tomography. *Rev Sci Instrum* August 2007;78(8):083706.
- [32] Carpenter CM, Rakow-Penner R, Jiang S, Pogue BW, Glover GH, Paulsen KD. Monitoring of hemodynamic changes induced in the healthy breast through inspired gas stimuli with MR-guided diffuse optical imaging. *Med Phys* April 2010;37(4):1638–46.
- [33] Masciotti JM, Lasker JM, Hielscher AH. Digital lock-in detection for discriminating multiple modulation frequencies with high accuracy and computational efficiency. *IEEE Trans Instrum Meas* 2008;57(1):182–9.
- [34] Ahmed N, Natarajan T, Rao KR. Discrete cosine transform. *IEEE Trans Comput* 1974;C-23:90–3.
- [35] Kim HK, Flexman M, Yamashiro DJ, Kandel JJ, Hielscher AH. PDE-constrained multispectral imaging of tissue chromophores with the equation of radiative transfer. *Biomed Optics Express* 2010;1(3):812–24.
- [36] Schaafsma BE, et al. Optical mammography using diffuse optical spectroscopy for monitoring tumor response to neoadjuvant chemotherapy in women with locally advanced breast cancer. *Clin Cancer Res* 2015;21(3):577–84.
- [37] Dehghani H, Pogue BW, Shudong J, Brooksby B, Paulsen KD. Three-dimensional optical tomography: resolution in small-object imaging. *Appl Optics* June 1, 2003;42(16):3117–28.
- [38] Pogue BW, Davis SC, Song X, Brooksby BA, Dehghani H, Paulsen KD. Image analysis methods for diffuse optical tomography. *J Biomed Optics* May-Jun;11(3):33001.
- [39] Chapman CB, Wasserman E. On the dynamic of the cardiac muscle, a translation of Otto Frank 'Zur Dynamik des Hertz Muskels'. *Zeitschrift für Biologie* 1895;32:370–447. *Am Heart J* 1959;58:282–487.
- [40] Sagawa K, Lie RK, Schaefer J. Translation of Otto Frank's paper Die Grundform des Arteriellen Pulses. *Zeitschrift Fur Biologie* 1899;37:483–526. *J Mol Cell Cardiol* March 1990;22(3):253–54.
- [41] Elad D, Einav S. Physical and flow properties of blood. In: *Standard handbook of biomedical engineering and design*. New York: McGraw-Hill; 2004.
- [42] Raines JK, Jaffrin MY, Shapiro AH. A computer simulation of arterial dynamics in the human leg. *J Biomech* 1974;7(1):77–91.
- [43] Stergiopoulos N, Young DF, Rogge TR. Computer simulation of arterial flow with applications to arterial and aortic stenoses. *J Biomech* December 1992;25(12):1477–88.
- [44] Tai NR, Giudiceandrea A, Salacinski HJ, Seifalian AM, Hamilton G. In vivo femoropopliteal arterial wall compliance in subjects with and without lower limb vascular disease. *J Vasc Surg* November 1999;30(5):936–45.

398 NEUROPHOTONICS AND BIOMEDICAL SPECTROSCOPY

- [45] Olufsen MS, Nadim A. On deriving lumped models for blood flow and pressure in the systemic arteries. *Math Biosci Eng* June 2004;1(1):61–80.
- [46] Shi Y, Lawford P, Hose R. Review of zero-D and 1-D models of blood flow in the cardiovascular system. *Biomed Eng Online* April 26, 2011;10:33.
- [47] Westerhof N, Lankhaar JW, Westerhof BE. The arterial Windkessel. *Med Biol Eng Comput* February 2009;47(2):131–41.
- [48] Tsanas A, et al. The Windkessel model revisited: a qualitative analysis of the circulatory system. *Med Eng Phys* June 2009;31(5):581–8.
- [49] Fragomeni G, Merola A, De Franciscis S, Amato F. A haemodynamic model of the venous network of the lower limbs. In: *Conf Proc IEEE Eng Med Biol Socvol. 2007; 2007. p. 1002–5.*
- [50] Stiukhina ES, Kurochkin MA, Klochkov VA, Fedosov IV, Postnov DE. Tissue perfusability assessment from capillary velocimetry data via the multicompartiment Windkessel model. In: *Saratov fall meeting 2014: optical technologies in biophysics and medicine XVI; laser physics and photonics XVI; and computational biophysics, Saratov, Russia, 2014: SPIE; 2015.*
- [51] Mashayekhi G, Zahedi E. Modeling blood flow & pressure in systemic circulation with cuff occlusion. In: *20th Iranian conference on biomedical engineering (ICBME 2013), Tehran, Iran, 2013: IEEE; 2014.*
- [52] Stergiopoulos N, Meister JJ, Westerhof N. Determinants of stroke volume and systolic and diastolic aortic pressure. *Am J Physiol* June 1996;270(6 Pt 2):H2050–9.
- [53] Boron WF, Boulpaep EL. *Medical physiology*. Philadelphia: Elsevier Saunders; 2005.
- [54] O'Rourke MF, Staessen JA, Vlachopoulos C, Duprez D, Plante GE. Clinical applications of arterial stiffness; definitions and reference values. *Am J Hypertens* May 2002;15(5):426–44.
- [55] Manning TS, Shykoff BE, Izzo Jr JL. Validity and reliability of diastolic pulse contour analysis (windkessel model) in humans. *Hypertension* May 2002;39(5):963–8.
- [56] Duprez DA, De Buyzere MM, De Bruyne L, Clement DL, Cohn JN. Small and large artery elasticity indices in peripheral arterial occlusive disease (PAOD). *Vasc Med* November 2001;6(4):211–4.
- [57] Pollak AW, Norton PT, Kramer CM. Multimodality imaging of lower extremity peripheral arterial disease: current role and future directions. *Circ Cardiovasc Imaging* November 2012;5(6):797–807.
- [58] Andreisek G, et al. Peripheral arteries in diabetic patients: standard bolus-chase and time-resolved MR angiography. *Radiology* February 2007;242(2):610–20.
- [59] A. C. Society. In: *Breast cancer facts & figures 2015–2016*. Atlanta, GA: I. American Cancer Society; 2015.
- [60] Thompson AM, Moulder-Thompson SL. Neoadjuvant treatment of breast cancer. *Ann Oncol* September 2012;23(Suppl 10):x231–6.
- [61] Rastogi P, et al. Preoperative chemotherapy: updates of National surgical adjuvant breast and bowel project protocols B-18 and B-27. *J Clin Oncol* February 10, 2008;26(5):778–85.
- [62] Heil J, et al. Diagnosis of pathological complete response to neoadjuvant chemotherapy in breast cancer by minimal invasive biopsy techniques. *Br J Cancer* December 1, 2015;113(11):1565–70.
- [63] von Minckwitz G, Fontanella C. Selecting the neoadjuvant treatment by molecular subtype: how to maximize the benefit? *Breast* August 2013;22(Suppl. 2):S149–51.
- [64] von Minckwitz G, et al. Response-guided neoadjuvant chemotherapy for breast cancer. *J Clin Oncol* October 10, 2013;31(29):3623–30.
- [65] Issa-Nummer Y, et al. Prospective validation of immunological infiltrate for prediction of response to neoadjuvant chemotherapy in HER2-negative breast cancer—a substudy of the neoadjuvant GeparQuinto trial. *PLoS One* 2013;8(12):e79775.

Chapter 14 • Dynamic Vascular Optical Tomographic Imaging 399

- [66] Untch M, von Minckwitz G. Neoadjuvant chemotherapy: early response as a guide for further treatment: clinical, radiological, and biological. *J Natl Cancer Inst Monogr* 2011;2011(43):138–41.
- [67] Khokher S, Mahmood S, Qureshi MU, Khan SA, Chaudhry NA. "Initial clinical response" to neoadjuvant chemotherapy: an in-vivo chemosensitivity test for efficacy in patients with advanced breast cancer. *Asian Pac J Cancer Prev* 2011;12(4):939–46.
- [68] Tromberg BJ, Pogue BW, Paulsen KD, Yodh AG, Boas DA, Cerussi AE. Assessing the future of diffuse optical imaging technologies for breast cancer management. *Med Phys* June 2008;35(6):2443–51.
- [69] Enfield LC, Gibson AP, Hebden JC, Douek M. Optical tomography of breast cancer-monitoring response to primary medical therapy. *Target Oncol* September 2009;4(3):219–33.
- [70] Busch DR, Choe R, Durduran T, Yodh AG. Toward noninvasive characterization of breast cancer and cancer metabolism with diffuse optics. *Pet Clin* 2013;8(3):345–65.
- [71] Herranz M, Ruibal A. Optical imaging in breast cancer diagnosis: the next evolution. *J Oncol* 2012;2012:863747.
- [72] Wang J, et al. In vivo quantitative imaging of normal and cancerous breast tissue using broadband diffuse optical tomography. *Med Phys* July 2010;37(7):3715–24.
- [73] Liedtke C, et al. Response to neoadjuvant therapy and long-term survival in patients with triple-negative breast cancer. *J Clin Oncol* March 10, 2008;26(8):1275–81.
- [74] Zhu Q, et al. Benign versus malignant breast masses: optical differentiation with US-guided optical imaging reconstruction. *Radiology* October 2005;237(1):57–66.
- [75] Flexman ML, et al. Monitoring early tumor response to drug therapy with diffuse optical tomography. *J Biomed Optics* January 2012;17(1):016014.
- [76] Ueda S, et al. Baseline tumor oxygen saturation correlates with a pathological complete response. *Canc Res* 2012;72(17):4318–28.
- [77] Jiang S, et al. Evaluation of breast tumor response to neoadjuvant chemotherapy with tomographic diffuse optical spectroscopy: case studies of tumor region-of-interest changes. *Radiology* August 2009;252(2):551–60.
- [78] Jiang S, et al. Predicting breast tumor response to neoadjuvant chemotherapy with Diffuse Optical Spectroscopic Tomography prior to treatment. *Clin Canc Res* 2014;20(23):6006–15.
- [79] Pakalnikies MG, et al. Tumor angiogenesis change estimated by using diffuse optical spectroscopic tomography: demonstrated correlation in women undergoing neoadjuvant chemotherapy for invasive breast cancer? *Radiology* 2011;259(2):365–74.
- [80] Busch DR, et al. Optical malignancy parameters for monitoring progression of breast cancer neoadjuvant chemotherapy. *Biomed Optics Express* January 1, 2013;4(1):105–21.
- [81] Choe R, et al. Differentiation of benign and malignant breast tumors by in-vivo three-dimensional parallel-plate diffuse optical tomography. *J Biomed Optics* Mar-Apr;14(2):024020.
- [82] Xu C, et al. Ultrasound-guided diffuse optical tomography for predicting and monitoring neoadjuvant chemotherapy of breast cancers recent progress. *Ultrason Imaging* January 2016;38(1):5–18.
- [83] Zhu Q, et al. Breast cancer: assessing response to neoadjuvant chemotherapy by using US-guided near-infrared tomography. *Radiology* 2013;266(2):433–42.
- [84] Zhu Q, et al. Utilizing optical tomography with ultrasound localization to image heterogeneous hemoglobin distribution in large breast cancers. *Neoplasia* March 2005;7(3):263–70.
- [85] Zhu Q, Tannenbaum S, Hegde P, Kane M, Xu C, Kurtzman SH. Noninvasive monitoring of breast cancer during neoadjuvant chemotherapy using optical tomography with ultrasound localization. *Neoplasia* October 2008;10(10):1028–40.

400 NEUROPHOTONICS AND BIOMEDICAL SPECTROSCOPY

- [86] Zhu Q, Wang L, Tannenbaum S, Ricci A, DeFusco P, Hegde P. Pathologic response prediction to neoadjuvant chemotherapy utilizing pretreatment near-infrared imaging parameters and tumor pathologic criteria. *Breast Cancer Res* 2014;16(5):456.
- [87] Cerussi A, et al. Predicting response to breast cancer neoadjuvant chemotherapy using diffuse optical spectroscopy. *Proc Natl Acad Sci USA* March 6, 2007;104(10):4014–9.
- [88] Soliman H, et al. Functional imaging using diffuse optical spectroscopy of neoadjuvant chemotherapy response in women with locally advanced breast cancer. *Clin Canc Res* May 1, 2010;16(9):2605–14.
- [89] Cerussi A, Tanamai VW, Hsiang D, Butler J, Mehta RS, Tromberg BJ. Diffuse optical spectroscopic imaging correlates with final pathological response in breast cancer neoadjuvant chemotherapy. *Philos Trans R Soc* 2011;369:4512–30.
- [90] Falou O, et al. Diffuse optical spectroscopy evaluation of treatment response in women with locally advanced breast cancer receiving neoadjuvant chemotherapy. *Transl Oncol* 2012;5(4):238–46.
- [91] Symmans WF, et al. Measurement of residual breast cancer burden to predict survival after neoadjuvant chemotherapy. *J Clin Oncol* October 1, 2007;25(28):4414–22.
- [92] Karahaliou A, Vassiou K, Arikidis NS, Skiadopoulos S, Kanavou T, Costaridou L. Assessing heterogeneity of lesion enhancement kinetics in dynamic contrast-enhanced MRI for breast cancer diagnosis. *Br J Radiol* 2010;83:296–306.
- [93] Fauzee NJ. Taxanes: promising anti-cancer drugs. *Asian Pac J Cancer Prev* 2011;12(4):837–51.
- [94] Minchinton AI, Tannock IF. Drug penetration in solid tumours. *Nat Rev Cancer* August 2006;6(8):583–92.
- [95] Griffon-Etienne G, Boucher Y, Brekken C, Suit HD, Jain RK. Taxane-induced apoptosis decompresses blood vessels and lowers interstitial fluid pressure in solid tumors: clinical implications. *Cancer Res* August 1, 1999;59(15):3776–82.
- [96] Kuo WH, et al. Vascularity change and tumor response to neoadjuvant chemotherapy for advanced breast cancer. *Ultrasound Med Biol* June 2008;34(6):857–66.
- [97] Taghian AG, et al. Paclitaxel decreases the interstitial fluid pressure and improves oxygenation in breast cancers in patients treated with neoadjuvant chemotherapy: clinical implications. *J Clin Oncol* March 20, 2005;23(9):1951–61.

Abstract

In this chapter we present latest advances in the area of dynamic optical tomographic imaging. In particular, we focus on clinical applications in diagnosing and monitoring peripheral artery disease and breast cancer.

Keywords:

Breast cancer; Medical imaging systems; Optical tomography; Peripheral artery disease; Vascular disease.